

*Supplementary Information*

*for*

**Multifunctional ionic porous frameworks for CO<sub>2</sub> conversion and combating microbes**

*MD. Waseem Hussain,<sup>a</sup> Vipin Bhardwaj,<sup>b</sup> Arkaprabha Giri,<sup>a</sup> Ajit Chande<sup>b\*</sup> Abhijit Patra<sup>a\*</sup>*

**<sup>a</sup>Department of Chemistry, Indian Institute of Science Education and Research Bhopal (IISERB), Bhopal, India -462066,**

**E-mail: abhijit@iiserb.ac.in**

**<sup>b</sup>Department of Biological Sciences, Indian Institute of Science Education and Research Bhopal (IISERB), Bhopal, India -462066,**

**E-mail: ajitg@iiserb.ac.in**

## Contents

	<b>Page No.</b>
<b>I. Instrumentation and methods</b>	3-4
<b>II. Fabrication of POFs and Zn/POFs</b>	
(a) Chemicals	5
(b) Synthesis of triaminoguanidinium chloride	5
(c) Fabrication of POFs	6
(d) Fabrication of Zn/POFs	6-7
(e) Synthesis of MTAG	7-8
<b>III. Characterizations of POFs and Zn/POFs</b>	
(a) Fourier transform infrared spectroscopic (FTIR) analysis	9-10
(b) Thermogravimetric analysis (TGA)	10-11
(c) Powder X-ray diffraction (PXRD) analysis	11-14
(d) Microscopic characterizations	15-17
(e) X-ray photoelectron spectroscopic (XPS) analysis	17-19
(f) Gas adsorption studies of POFs and Zn/POFs	20-23
<b>IV. CO<sub>2</sub> conversion catalyzed by POFs and Zn/POFs</b>	
Optimization of reaction conditions, mechanism, recyclability	24-25
<b>V. Antibacterial and antiviral applications with POFs and Zn/POFs</b>	
(a) Antibacterial activity analysis	26-28
(b) Bacterial biofilm formation	29
(c) Antibacterial film coating	29-30
(d) SYBR Green-I and propidium iodide staining	30-31
(e) Water purification	32-33
(f) Bradford assay	33-34
(g) Virus production	34-36
(h) Cytotoxicity analysis using cell counting assay	36
(i) Virus lysis assay	37
<b>VI. Comparative tables</b>	
Comparative accounts of metal/metal oxide loading capacities (wt%) of Zn/POFs with various porous materials	38-39
Comparative accounts of POFs and Zn/POFs with other porous materials for CO <sub>2</sub> conversion	40-41
Comparative accounts of POFs and Zn/POFs with other notable porous materials for multifunctional applications	42
Comparison of antibiofilm application of POF2 and Zn/POF2 with some of the representative polymers, MOFs, metal nanoparticles and composites	43-45
<b>VII. Nuclear magnetic resonance (NMR) spectra</b>	46-51
<b>VIII References</b>	52-55

## I. Instrumentation and methods

---

**Nuclear magnetic resonance (NMR) spectroscopy:** Bruker Avance III 500 MHz NMR spectrometer was used to check the solution state  $^1\text{H}$  NMR spectra. The residual solvent signals were used as internal standard, and chemical shifts ( $\delta$ ) were reported in parts per million (ppm). The yields of the cyclic carbonates during catalysis were calculated using 1,1,2,2-tetrachloroethane as an external NMR standard. The solid-state  $^{13}\text{C}$  cross-polarization magic angle spinning (CP/MAS) NMR experiments were carried out on JEOL ECX2 400 MHz (field 9.4 T) standard bore spectrometer equipped with 4 mm solid-state MAS probe. The samples were packed into a 4 mm Zirconia rotor and spun at 8 kHz at the magic angle.

**Fourier transform infrared spectroscopy (FTIR):** Perkin-Elmer Model 2000 FTIR was used to measure the FTIR spectra of the samples using KBr pellet. Twenty scans were signal-averaged, with a resolution of  $8\text{ cm}^{-1}$  at ambient temperature.

**Thermogravimetric analysis (TGA):** Perkin Elmer TGA-6000 instrument was used to carry out TGA of the samples. The sample was heated from  $30\text{ }^\circ\text{C}$  to  $900\text{ }^\circ\text{C}$  under the nitrogen atmosphere at a scan rate of  $10\text{ }^\circ\text{C min}^{-1}$ .

**Powder X-ray diffraction (PXRD):** PANalytical Empyrean XRD instrument was used to carry out the PXRD experiment. Data was collected for  $2\theta$  values ranging from  $5^\circ$  to  $60^\circ$ .

**Field emission scanning electron microscopy (FESEM):** The surface morphology of all polymers was examined using a Carl Zeiss (Ultraplus) field emission scanning electron microscope. Samples for microscopy were prepared by dispersing  $\sim 0.5\text{ mg}$  of the sample in  $2\text{ mL}$  of MeOH and drop-casting the dispersion on to a silicon wafer covered with adhesive carbon tape. All samples were coated with a thin layer of sputtered gold before imaging. FESEM was carried out using an accelerating voltage of  $5\text{ kV}$  and  $10\text{ kV}$ .

**Transmission electron microscopy (TEM):** The morphology of the polymers was examined using FEI TALOS 200S instrument at a working voltage of  $200\text{ kV}$ . The samples for TEM analysis were prepared by drop-casting a homogeneous dilute MeOH dispersion of the polymers over a carbon-coated 400 mesh Cu grid.

**Energy dispersive X-ray spectroscopy (EDS)** was carried out at a working voltage of  $200\text{ kV}$  using Cu as a reference.

**Gas adsorption studies:** All the gas adsorption measurements were performed on Quantachrome Autosorb QUA211011 equipment. The temperature was maintained using liq.  $\text{N}_2$  for measurements

at 77 K and chiller bath for measurements at 273 K and 298 K. Isotherms were analyzed using ASIQwin software. All the samples were treated at 100 °C for 24 h under high vacuum for the degassing before the analysis.

**X-ray photo electron spectroscopy (XPS):** The XPS experiment was performed using PHI 5000 Versa Prob II, FIE Inc on a sample holder with a vacuum-dried powder sample drop of the size 1.5 mm radius. The scan time was set for 1 h per element for core level scan (energy band: 20 eV) with a pass setting of 23.5 eV. 0.025 eV step and 100 ms time per step for 5 cycles were followed.

**Inductively coupled plasma optical emission spectrometry (ICP-OES):** Zn/POF2 before and after catalytic conversion of CO<sub>2</sub> and epoxide into cyclic organic carbonates was subjected to ICP-OES analysis to quantify the metal leaching. 10 mg of each sample digested in conc. HCl (diluted to 10<sup>3</sup>-fold), and were analysed for the amount of Zn present in the catalyst.

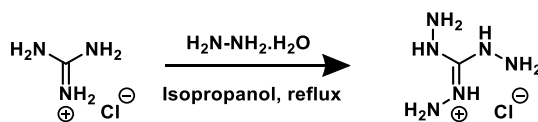
## II. Fabrication of POFs and Zn/POFs

### (a) Chemicals

All the chemicals were used as received unless stated otherwise. Guanidine hydrochloride ( $\geq 99\%$ ), hydrazine hydrate (50-60%), benzene-1,3,5-tricarboxaldehyde (97%), terephthalaldehyde (99%), 1,2-dichlorobenzene (99%), 1-butanol (99.8), acetic acid ( $\geq 99\%$ ), tetrabutylammonium bromide ( $\geq 99\%$ ), ( $\pm$ )-propylene oxide ( $\geq 99.5\%$ ), zinc acetate dihydrate ( $\geq 98\%$ ) were received from Sigma-Aldrich. 1,1,2,2-Tetrachloroethane was received from Sigma-Aldrich and used as an external standard for the % yield calculations.

### (b) Synthesis of triaminoguanidium chloride (TAG)

The monomer TAG was synthesized following a reported procedure (Scheme S1).<sup>1</sup> Typically, guanidium chloride (1 mmol) was taken in 30 mL of isopropanol in a 100 mL round bottom flask. To the above-stirred solution, 50-60% hydrazine hydrate (4.5 mmol) was added and stirred to reflux for 6 h. After the reaction, the formed precipitate was filtered and washed with 50 mL of isopropanol to yield 97% of triaminoguanidium chloride.



**Scheme S1** Synthetic protocol of TAG.

**MALDI-TOF:** Calculated  $m/z$  for  $\text{C}_1\text{N}_6\text{H}_{10}$  [ $\text{M}^+$ ] 140.57, found [ $\text{M}+5\text{H}^+$ ] 145.68.

We checked the crystal structure of TAG to confirm the formation of the product. The molecular structure obtained from the crystal structure [space group:  $P6_3/m$ , unit cell dimensions:  $a = 7.4862(9)$  Å,  $b = 7.4862(9)$  Å,  $c = 6.2347(8)$  Å,  $\alpha = 90^\circ$ ,  $\beta = 90^\circ$ ,  $\gamma = 120^\circ$ ] analysis was found to be similar to the reported one.<sup>2</sup>

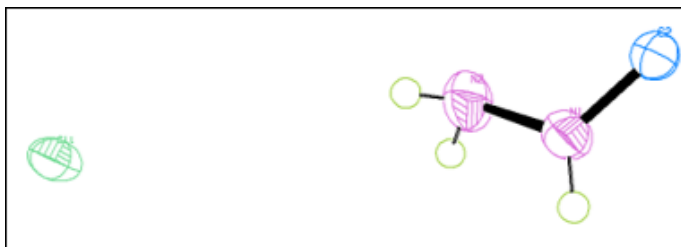
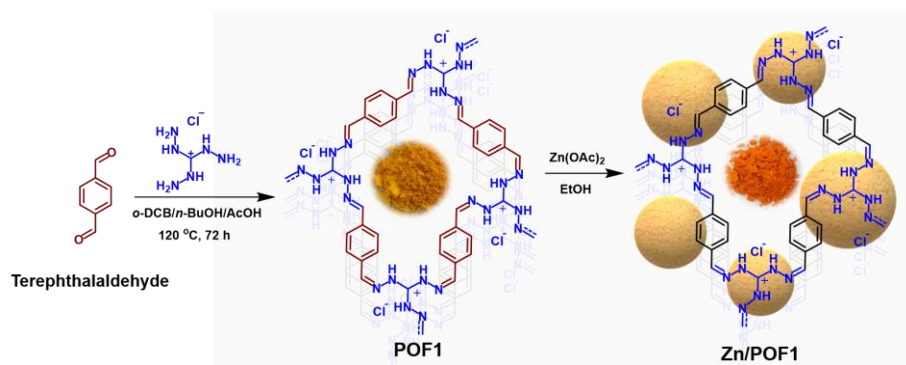


**Fig. S1** ORTEP diagram of TAG at 50% ellipsoid probability level crystallized in the  $P6_3/m$  space group.

## (c) Fabrication of POFs

### (i) Fabrication of POF1

In a typical synthesis (Scheme S2), a mixture of TAG (0.31 mmol) and terephthalaldehyde (0.53 mmol) was degassed in a Schlenk tube. A mixture of *o*-dichlorobenzene (5 mL), *n*-butanol (5 mL), and acetic acid (1 mL) was degassed using 3 cycles of freeze-pump-thaw and was added to the reaction mixture under an inert atmosphere of argon. The reaction was allowed to continue for 72 h. Later, the reaction mixture was washed with MeOH (excess) and then filtered. The collected residue was further subjected to Soxhlet extraction using methanol, acetone, and chloroform each for 24 h. A yellowish solid was collected and subjected to extensive drying. Yield: 95%.



**Scheme S2** Synthetic protocol of POF1 and Zn/POF1 (crystallite/particle size of ZnO is not to scale as per the pore sizes of the frameworks in the pictorial depiction).

### (ii) Fabrication of POF2

A mixture of TAG (0.31 mmol), 1,3,5-benzene-tricarboxaldehyde (0.31 mmol) was degassed in a Schlenk tube. A mixture of *o*-dichlorobenzene (5 mL), *n*-butanol (5 mL), and acetic acid (1 mL) was degassed using 3 cycles of freeze-pump-thaw and was added to the reaction mixture under an inert atmosphere of argon. The reaction was allowed to continue for 72 h. Later, the reaction mixture was washed with MeOH (excess) and then filtered. The collected residue was further subjected to Soxhlet extraction using methanol, acetone, and chloroform each for 24 h. A greenish-yellow solid was collected and subjected to extensive drying (Fig. 1a). Yield: 92%.

## (d) Fabrication of Zn/POFs

### (i) Fabrication of Zn/POF1

In a typical synthesis (Scheme S2), 50 mg of POF1 was added to Zn(OAc)<sub>2</sub> solution in EtOH (10 wt.% in EtOH) and was degassed with vacuum-argon cycles for 3 times. The reaction mixture was allowed to stir at 90 °C for 12 h under argon atmosphere. The solid was collected

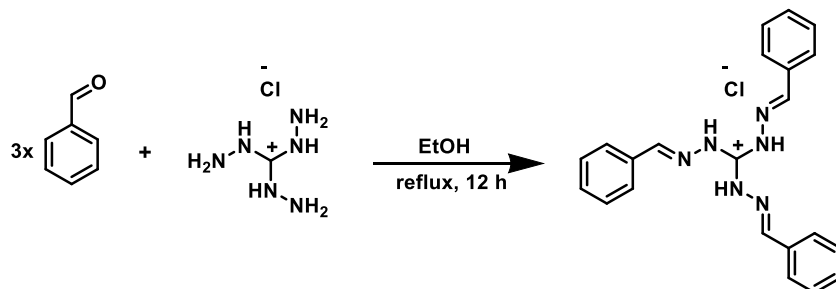
through filtration and subjected to Soxhlet purification using MeOH and CHCl<sub>3</sub> each for 24 h. The yellow color solid was dried at 100 °C in a glass-oven under vacuum.

### (ii) Fabrication of Zn/POF2

A similar procedure was followed for the fabrication of Zn/POF2 (Fig. 1a), as mentioned above, for Zn/POF1.

### (e) Synthesis of MTAG

The synthesis of the model compound based on TAG was carried out following the procedure mentioned below (Scheme S3). To the solution of benzaldehyde (1.06 mmol) in 10 mL of EtOH, few drops of conc. HCl was added and stirred for 2 mins at room temperature. Then 0.35 mmol of TAG was added to the above solution and allowed to stir at 70 °C for 12 h. After the reaction, the solvent was evaporated, and the resultant solid was washed with diethyl ether and then dried under the vacuum. Yield 90%. <sup>1</sup>H NMR (500 MHz, CDCl<sub>3</sub>) δ (ppm): 11.39 (3 H, s), 8.68 (3 H, s), 7.92 (6 H, s), 7.42 (9 H, s). <sup>13</sup>C NMR (126 MHz, CDCl<sub>3</sub>) δ (ppm): 151.46, 147.99, 132.78, 130.99, 128.76, 128.65. MALDI-TOF: Calculated m/z for C<sub>22</sub>H<sub>22</sub>N<sub>6</sub> [M<sup>+</sup>] 369.45, found 369.14.



**Scheme S3** Synthetic protocol for the model compound of POF2 (MTAG).

**Crystallographic details of MTAG:** Crystals of MTAG were obtained by slow evaporation from acetonitrile solution. The structural details are mentioned below (Table S1, CCDC No. 1966910).

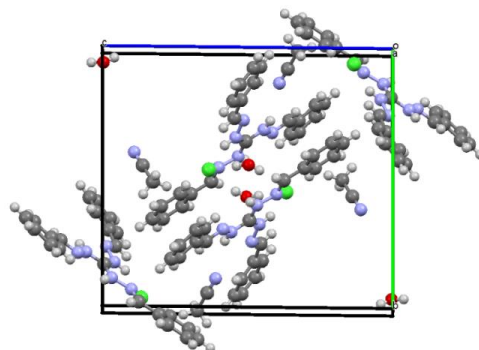


**Fig. S2** The crystal structure packing of the model compound for POF2 (MTAG) (C: grey, N: blue, Cl: green, H: white).

**Table S1** Crystal data and structure refinement for MTAG (CCDC No. 1966910)

Empirical formula	C <sub>22</sub> H <sub>21</sub> N <sub>6</sub> Cl, C <sub>2</sub> H <sub>3</sub> N, H <sub>2</sub> O
Formula weight	505.0283
Temperature	296(2) K
Wavelength	0.71073 Å
Crystal system	Monoclinic
Space group	<i>P</i> 2 <sub>1</sub> / <i>c</i>
Unit cell dimensions	a = 8.6917(2) Å, b = 15.6895(5) Å, c = 17.8706(6) Å, α = 90°, β = 101.494(2)° and γ = 90°
Volume	2388.11(12) Å <sup>3</sup>
Z	4
Density (calculated)	1.405 mg/m <sup>3</sup>
Absorption coefficient	0.211 mm <sup>-1</sup>
F(000)	1088
Crystal size	0.22 x 0.18 x 0.12 mm <sup>3</sup>
Theta range for data collection	1.743 to 30.741°
Index ranges	-11 ≤ h ≤ 12, -22 ≤ k ≤ 22, -23 ≤ l ≤ 25
Reflections collected	27187
Independent reflections	7340 [R(int) = 0.0501]
Completeness to theta = 25.242°	99.9 %
Absorption correction	None
Refinement method	Full-matrix least-squares on F <sup>2</sup>
Data / restraints / parameters	7340 / 0 / 302
Goodness-of-fit on F <sup>2</sup>	1.056
Final R indices [I > 2σ(I)]	R1 = 0.0671, wR2 = 0.1643
R indices (all data)	R1 = 0.1170, wR2 = 0.1923
Largest diff. peak and hole	0.737 and -0.298 e.Å <sup>-3</sup>



### III. Characterization of POFs and Zn/POFs

#### (a) Fourier transform infrared spectroscopic (FTIR) analysis

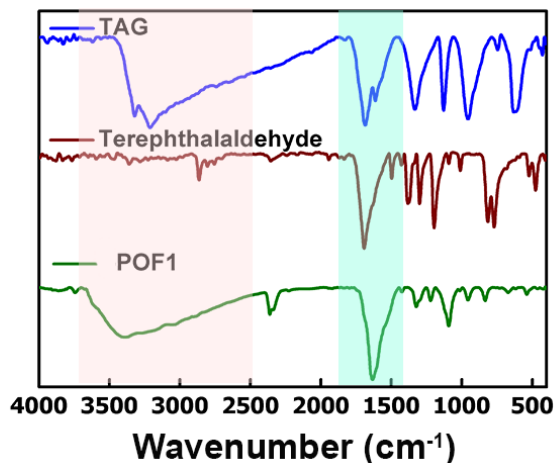


**Fig. S3** FTIR spectra of TAG (blue), terephthalaldehyde (brown), and POF1 (green).

The FTIR spectra of respective monomers along with that of POF1 and POF2 are shown in Fig. S3 and S4, respectively. The C=N stretching at  $1632\text{ cm}^{-1}$  indicates the cross-condensation between the monomers. The peak at  $1102\text{ cm}^{-1}$  can be assignable to the C-N stretching of the TAG unit. Further, a new peak appears at  $462\text{ cm}^{-1}$  that refers to the formation of ZnO in Zn/POF2 (Fig. 1b). The shift of the peak at  $1632\text{ cm}^{-1}$  in pristine POFs to  $1566\text{ cm}^{-1}$  in Zn/POFs refers to the decrease in the bond length of C=N after the ZnO loading suggesting the metal coordination in the polymer framework (Fig. S5, 1b).

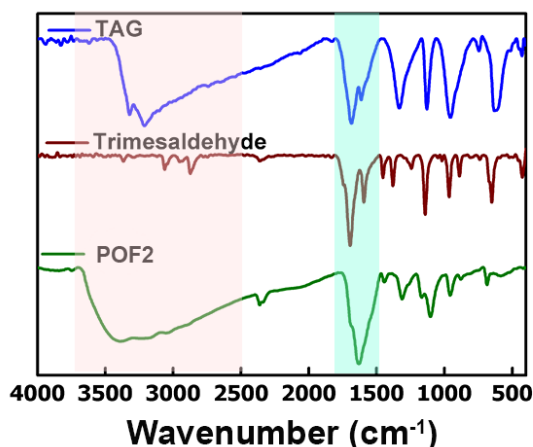


**Fig. S4** FTIR spectra of TAG (blue), trimesaldehyde (benzene-1,3,5-tricarboxaldehyde, brown), and POF2 (green).

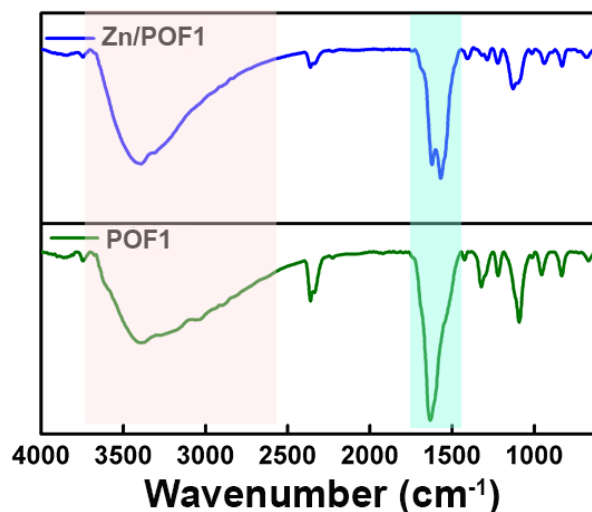


**Fig. S5** FTIR spectra of Zn/POF1 (blue), and POF1 (green).

### (b) Thermogravimetric analysis (TGA)

The thermogravimetric analysis of POFs revealed that the POFs were stable up to  $\sim 250$  °C. The amount of the ZnO loading in Zn/POFs was further confirmed by the TGA analysis (Fig. 1c, S6). The variation of the ZnO loading in Zn/POFs, in samples obtained through different batches of fabrication was examined (Fig. S6) and ZnO amount in Zn/POF2 was found to be  $57.3 \pm 1.2$  wt%. Further, the TGA of the sample after the hot filtration experiment was performed to confirm no significant metal leaching (Fig. S7).

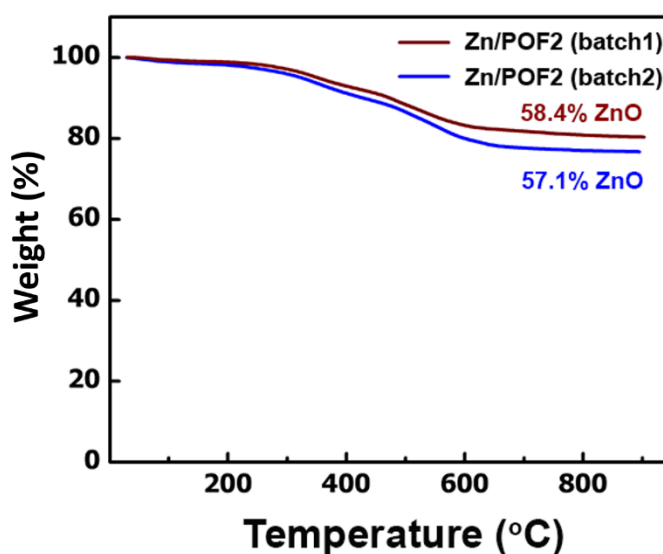


**Fig. S6** The thermogravimetric analysis of Zn/POF2 obtained through different batches of synthesis, indicating the high loading of ZnO.

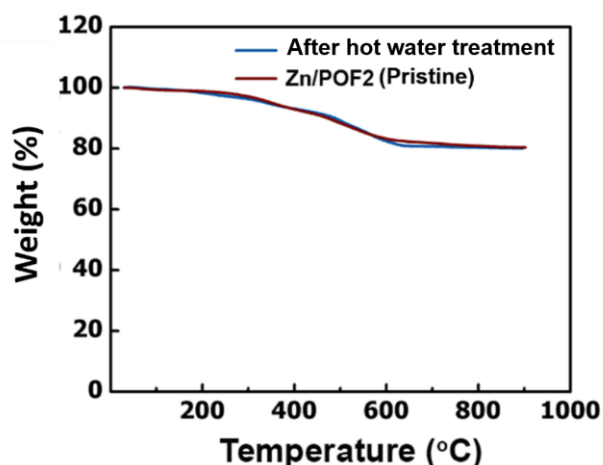


**Fig. S7** Thermogravimetric analysis of Zn/POF2 before (brown) and after the hot water treatment (blue).

### (c) Powder X-ray diffraction (PXRD) analysis

The structure modelling of the POFs was performed using the Reflex module implemented in Materials Studio 6.1 software package (Fig. S8a, S8b). The unit cell dimension was first determined by the observed powder X-ray diffraction peak positions. Further, the cell was optimized using Pawley refinement constructed in the module until the  $R_{wp}$  value converges ( $R_{wp}$

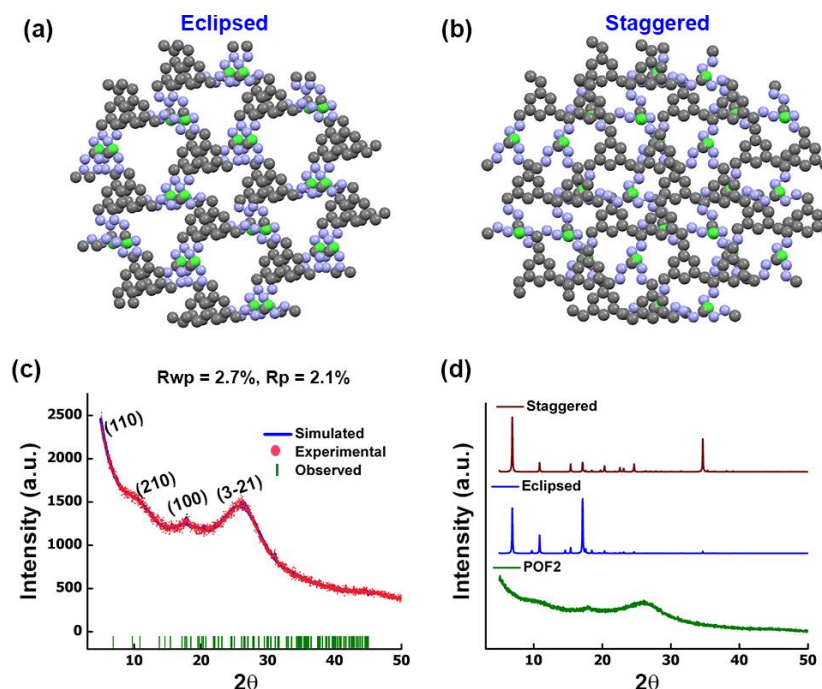


**Fig. S8** Modelled structures of POF2 in (a) eclipsed and (b) staggered conformation. (c) The simulated PXRD (blue), experimental PXRD pattern (red) as well as the observed peaks (green) for POF2 using Materials Studio 6.1. (d) The comparative analysis of powder X-ray diffraction patterns of POF2 with the modelled PXRD patterns (eclipsed as well as staggered forms).

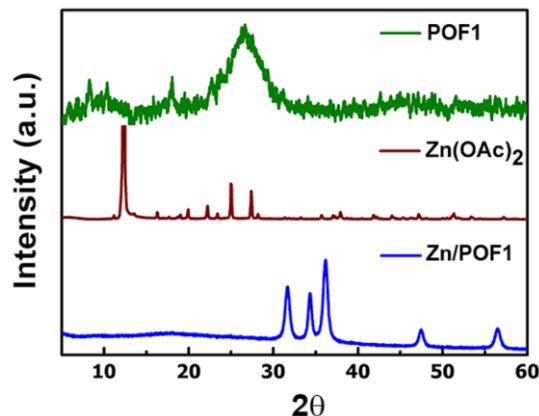


**Fig. S9** The PXR D of POF1 (green), Zn(OAc)<sub>2</sub> (brown), and Zn/POF1 (blue).

= 2.7% and  $R_p = 2.1\%$ ). The experimental PXR D indexing for POF2 revealed a tetragonal system with the lattice parameters  $a = 18.18$ ,  $b = 18.18$ ,  $c = 5.17$ ,  $\alpha = 90^\circ$ ,  $\beta = 90^\circ$  and  $\gamma = 90^\circ$  (Fig. S8c). The conformations (eclipsed as well as staggered) of POFs were modelled in the Materials Studio with an interplanar spacing of  $3.6 \text{ \AA}$  with a  $P4$  space group that showed similarity with the experimental PXR D data. The results suggested the presence of both eclipsed as well as staggered conformations that led to the broadening of the PXR D pattern (Fig. S8d). The low crystallinity of TAG-based POFs is likely due to the electrostatic repulsion between the two layers of cationic triaminoguanidinium units and intercalated chloride ions leading to the poor  $\pi$ - $\pi$  stacking.<sup>2,3</sup>

The powder X-ray diffraction analysis was carried out, collecting the data at a  $2\theta$  range of  $5^\circ$  to  $60^\circ$ . The broad pattern of the peak signifies the amorphous nature of the polymer. The incorporation of ZnO in Zn/POF2 was further confirmed by the peaks at  $2\theta$  equals to  $31.7^\circ$ ,  $34.3^\circ$ ,  $36.2^\circ$ ,  $47.4^\circ$ , and  $56.5^\circ$  that correspond to the planes (100), (020), (101), (102) and (110) of ZnO,

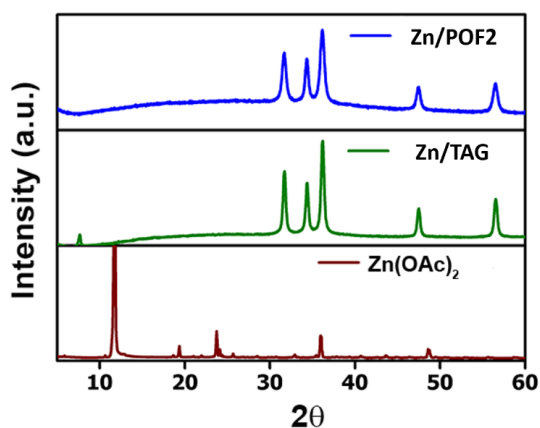


**Fig. S10** The PXR D analysis of the samples after refluxing Zn(OAc)<sub>2</sub> with only ethanol (brown), in the presence of TAG (Zn/TAG, green), and POF2 (Zn/POF2, blue) in ethanol indicating the role of triaminoguanidinium core (TAG) for the formation of ZnO.

respectively in the würtzite form (Fig. 1d). Owing to the heterogeneous nature of the reaction medium, it is difficult to examine the exact reaction mechanism for the formation of ZnO from the precursor Zn(OAc)<sub>2</sub>. However, for the qualitative elucidation of the mechanism, we performed a number of control experiments. We carried out a similar reaction in the absence of POFs, where we observed, there was no formation of ZnO (Fig. S10). It is obvious because in the absence of base/acid, the hydrolysis of Zn(OAc)<sub>2</sub> is not possible to occur.<sup>4</sup> Similarly, taking triaminoguanidinium chloride (TAG-Cl) in the reaction mixture instead of POF, we observed the formation of ZnO, as proved by PXRD analysis (Fig. S10). These results indicate that there is a profound role of triaminoguanidinium-based POFs and more precisely the *N*-rich guanidinium core for the formation of ZnO. The PXRD analysis of Zn/POFs indicated the crystallite size in the range of 11-15 nm. The ZnO particles were impregnated with the network. Even though we could observe the fringe pattern from the TEM images, but the discrimination of ZnO from the network was not possible.

Based on the above experimental evidence, we proposed a plausible mechanism for the *in situ* formation of ZnO from Zn(OAc)<sub>2</sub> facilitated by the *N*-rich network (Fig. S11). The following mechanism illustrates that in the steps (i), (ii) and (iii), the intermediate species of mono and disubstituted Zn-complex are formed. A similar mode of complexation of triaminoguanidinium-based ligands with different metal ions (e.g., Zn<sup>2+</sup>) was also anticipated by us as well as reported in previous literature.<sup>1,4</sup> In the final step (i.e., step iv), a condensation between intermediate Zn(II)-complexes (step ii, iii) leading to the elimination of water and formation of polymeric -O-Zn-O-Zn-O- species is presumed. The mechanism of formation of ZnO infused POFs was proposed considering the mechanistic illustration presented in the earlier literature.<sup>5</sup> Here, the POFs not only act as the catalyst but also as the template. However, the validity of the mechanism of the *in situ* formation of ZnO is intriguing and can be a subject of further experimental exploration.

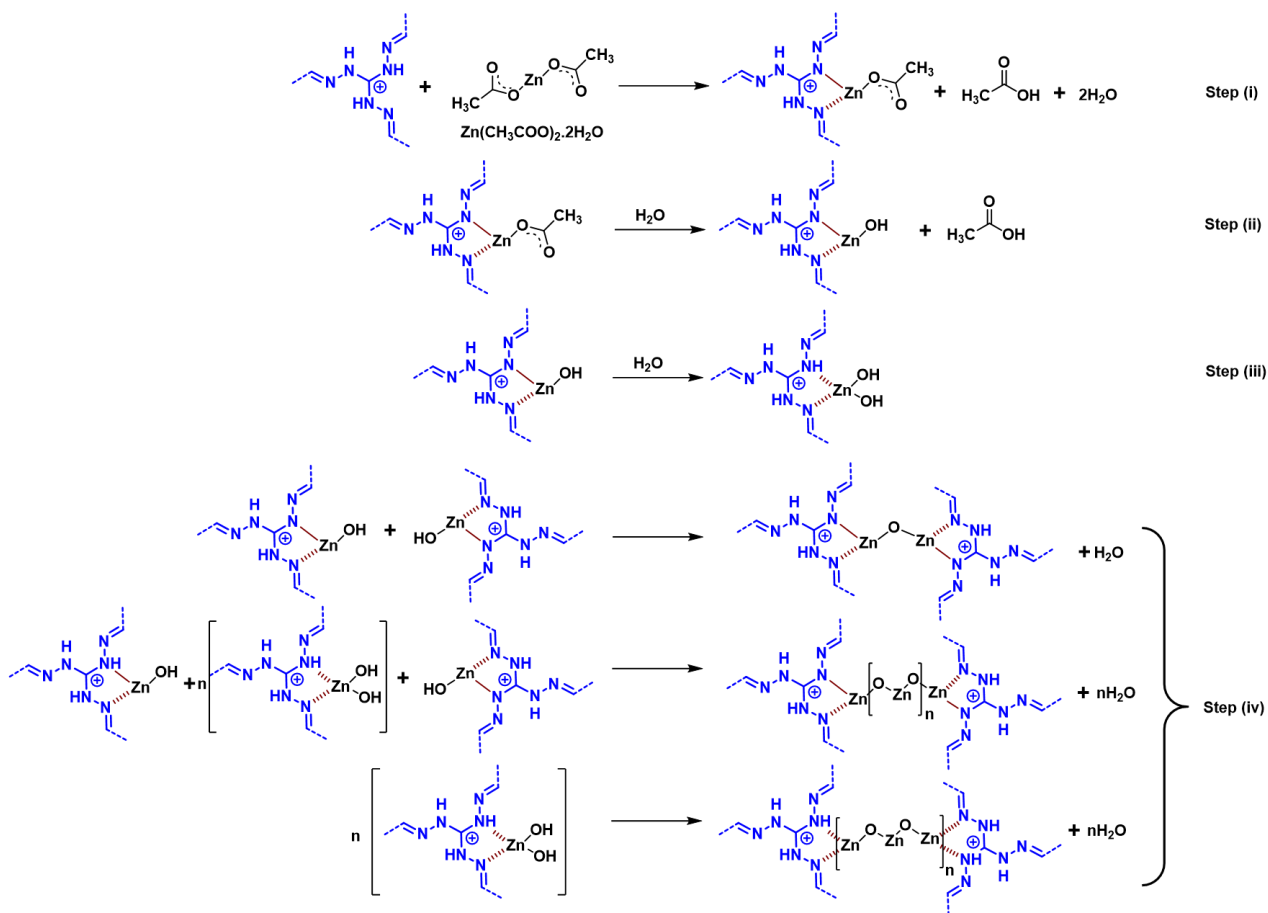


**Fig. S11** The plausible mechanism depicting the *in situ* formation of ZnO infused triaminoguanidinium framework (dotted lines between N and Zn atoms represent stabilizing interaction(s)).

#### (d) Microscopic characterizations

The field emission scanning electron microscopy (FESEM) image of POF2 (Fig. S12a) illustrates the formation of granular morphology like microstructures (composed of small spherical aggregates). Whereas, the formation of agglomerates of the irregular granular morphology was observed in the case of Zn/POF2 (Fig. S12b). The transmission electron microscopy (TEM) images revealed the porous nature of POF2 and Zn/POF2 (Fig. S14a, S14b, respectively). The EDS analysis was carried out for POF2 and Zn/POF2 (Fig. S15). Further, the uniform distribution of ZnO in Zn/POF2 was confirmed by the high-angle annular dark-field scanning transmission electron microscopy (HAADF-STEM) elemental mapping (Fig. S16).

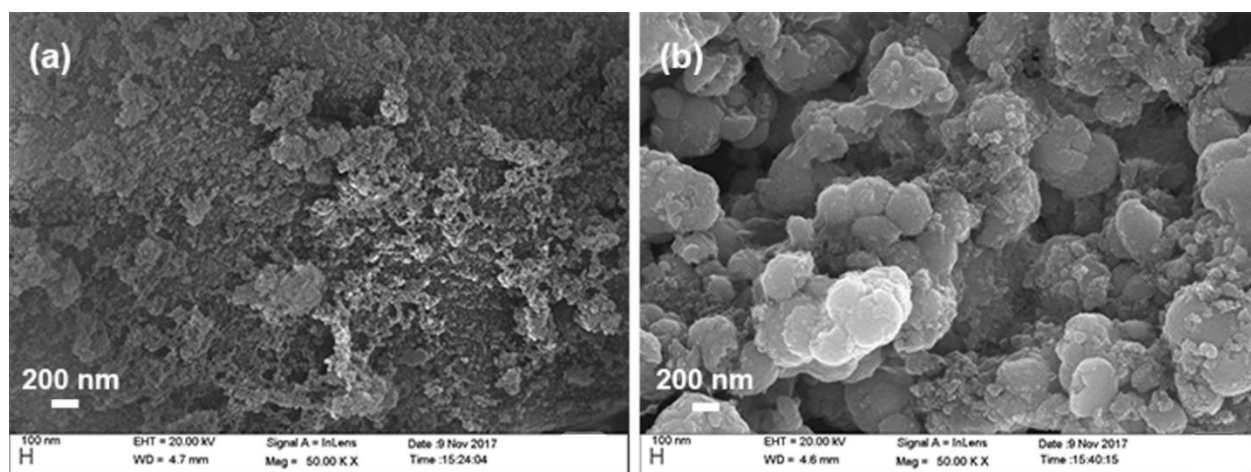


**Fig. S12** FESEM images of (a) POF2 and (b) Zn/POF2.

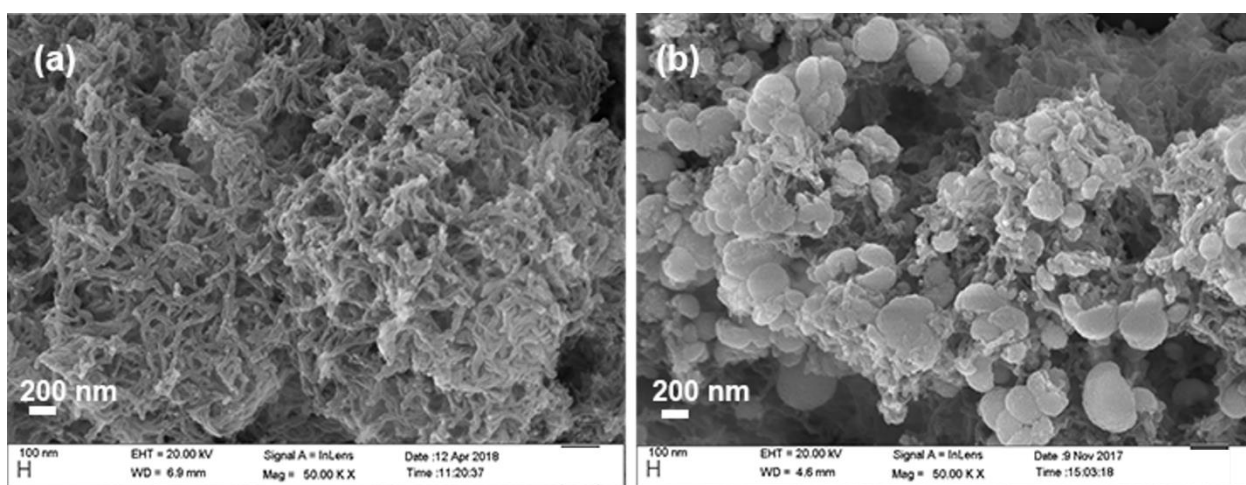


**Fig. S13** FESEM images of (a) POF1 and (b) Zn/POF1.

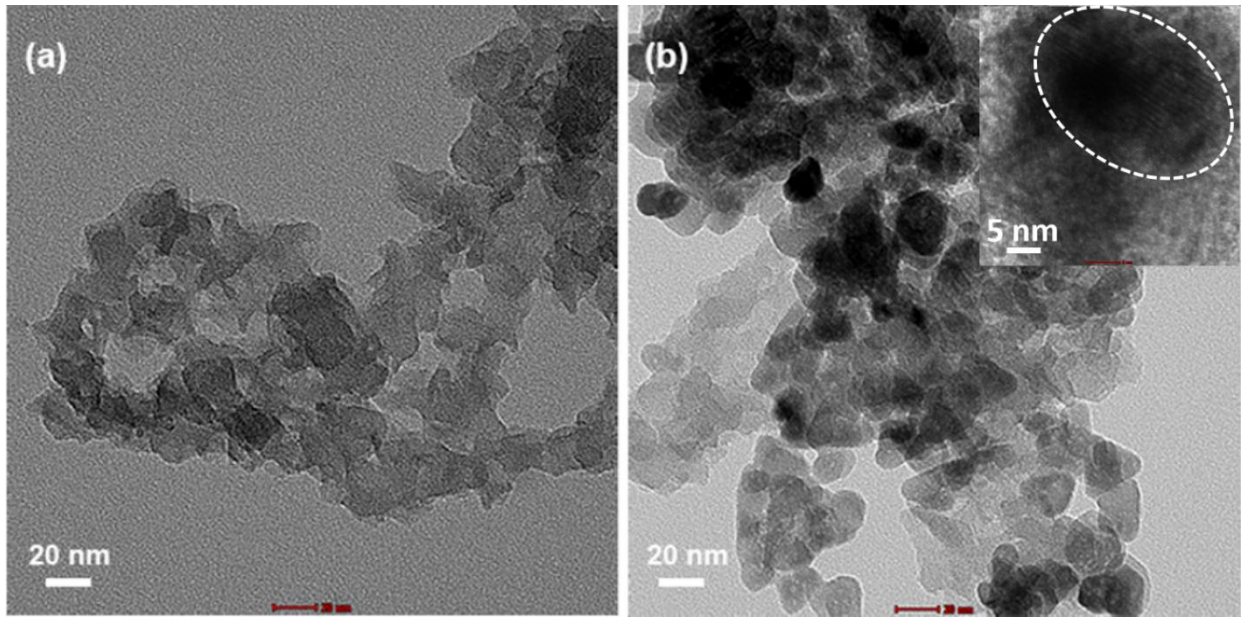


**Fig. S14** TEM images of (a) POF2 and (b) Zn/POF2 (scale bar = 20 nm); inset: the fringe pattern in Zn/POF2 due to the infused ZnO matrix (scale bar = 5 nm).

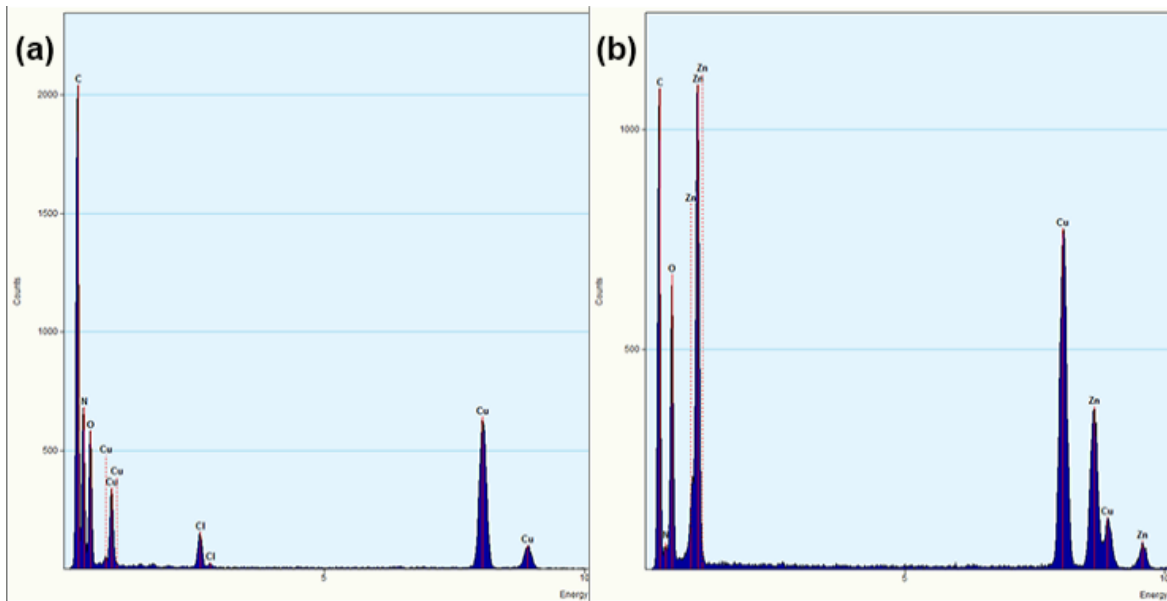


**Fig. S15** The EDS analysis of (a) POF2 and (b) Zn/POF2 showing the elemental distribution.



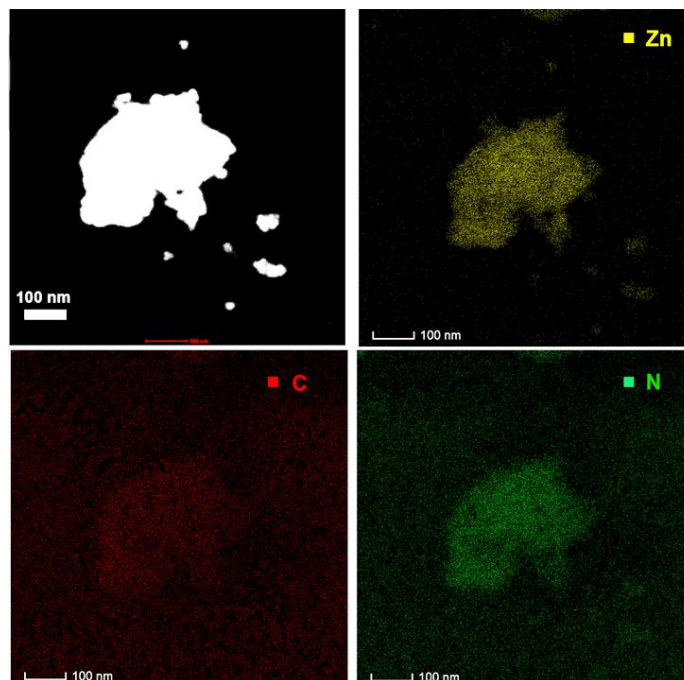


**Fig. S16** High-angle annular dark-field scanning transmission electron microscopy (HAADF-STEM) elemental mapping images of Zn/POF2 [ Zn (yellow), C (red), and N (green)].

### (e) X-ray photoelectron spectroscopic (XPS) analysis

The XPS analysis of POFs and Zn/POFs are shown in Fig. S17-S19. The peak at 530.2 eV in the O1s XPS spectrum was taken as the reference for the calculation of the amount of ZnO loading in Zn/POFs (Fig. S18d). All the nitrogen atoms of triaminoguanidinium in POFs are in a similar chemical environment due to the extensive resonating structure. It is evident by the single peak of N1s (B.E. = 398.44 eV, before metal loading) in the X-ray photoelectron spectroscopy (XPS) (Fig. S17b). After the metal loading, the N1s XPS showed a single peak at 398.01 eV in Zn/POF2 (Fig. S18b). Even though the N1s XPS spectrum revealed a slight shift due to the interaction with ZnO, no splitting was observed, presumably due to the conjugation. Similar kinds of results were observed in the recent reports for the N1s high-resolution XPS spectra of POFct-1 before and after adsorbing Hg(II) and Cu(II),<sup>6a</sup> and also for N1s in PFe<sub>3</sub>O<sub>4</sub>@NH<sub>2</sub>-MIL-125 before and after Pb(II) adsorption.<sup>6b</sup> Inward contraction of N-valence electrons takes place due to the metal-N coordination. Thereby N1s core electron experiences more screening compared to the pristine N, and consequently, resulting in the smaller binding energy of the N1s core level.<sup>6c</sup> It is to be noted that an upfield shift of the aldimine protons of the triaminoguanidinium Schiff base in the solution-state <sup>1</sup>H NMR spectra while titration with Zn<sup>2+</sup>/ Cd<sup>2+</sup> was observed in earlier work asserting coordination of Zn(II) with triaminoguanidinium core.<sup>1,6d</sup>

However, a clear distinction was observed in the guanidinium C, imine C and phenylic C of POFs and Zn/POFs. The C1s XPS spectra of POFs revealed the presence of three types of C (phenylic: 282.8 eV; imine: 284.0 eV; guanidinium: 286.6 eV) with distinct distributions (Fig. S17a). Whereas, in Zn/POFs, a significant change in XPS spectra was observed due to the interaction with ZnO [POF2: 59.6% (phenylic-C); 31.3% (imine-C); 8.9% (guanidinium-C), Zn/POF2: 63.5% (283.1 eV, phenylic-C); 31.3% (283.9 eV, imine-C); 5.0% (287.1 eV, guanidinium-C), Fig. 1i, S17a, S18a]. Furthermore, the shift of the peak at 1632  $\text{cm}^{-1}$  in POFs to 1566  $\text{cm}^{-1}$  in Zn/POFs indicates the increase of C=N bond length due to the ZnO loading, signifying the coordination with the framework (Fig. 1b, S5). The stability and recyclability of Zn/POFs in catalysis further support the same (*vide infra*).

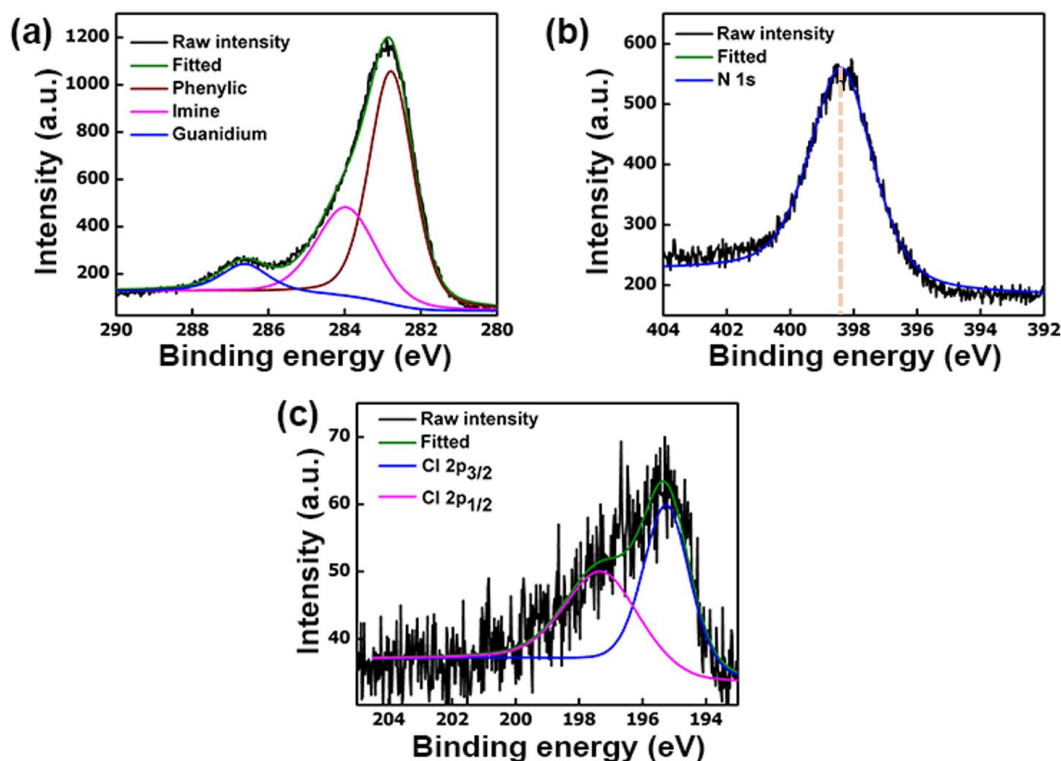


**Fig. S17** The XPS analysis of POF2 for (a) C1s, (b) N1s, and (c) Cl2p, respectively.

**Table S2** Atomic (at.) % of carbon, nitrogen, zinc, and oxygen, acquired from XPS analysis.

Substance	C	N	Zn	O
POF1	81.1	17.4	-	-
Zn/POF1	47.4	12.2	17.4*	17.4
POF2	70.9	26.9	-	-
Zn/POF2	47.6	14.9	16.5*	16.5

\*Percentage of Zn calculated by taking the O1s XPS analysis.

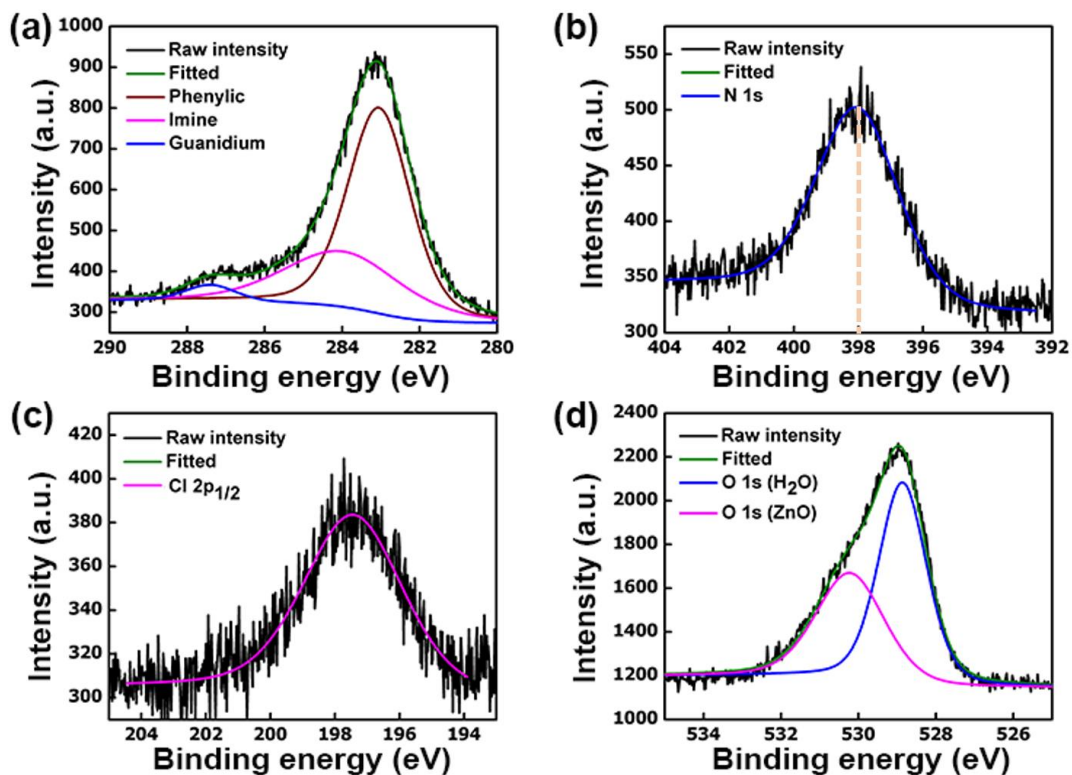


Fig. S18 The XPS analysis of Zn/POF2 for (a) C1s, (b) N1s, (c) Cl2p, and (d) O1s, respectively.

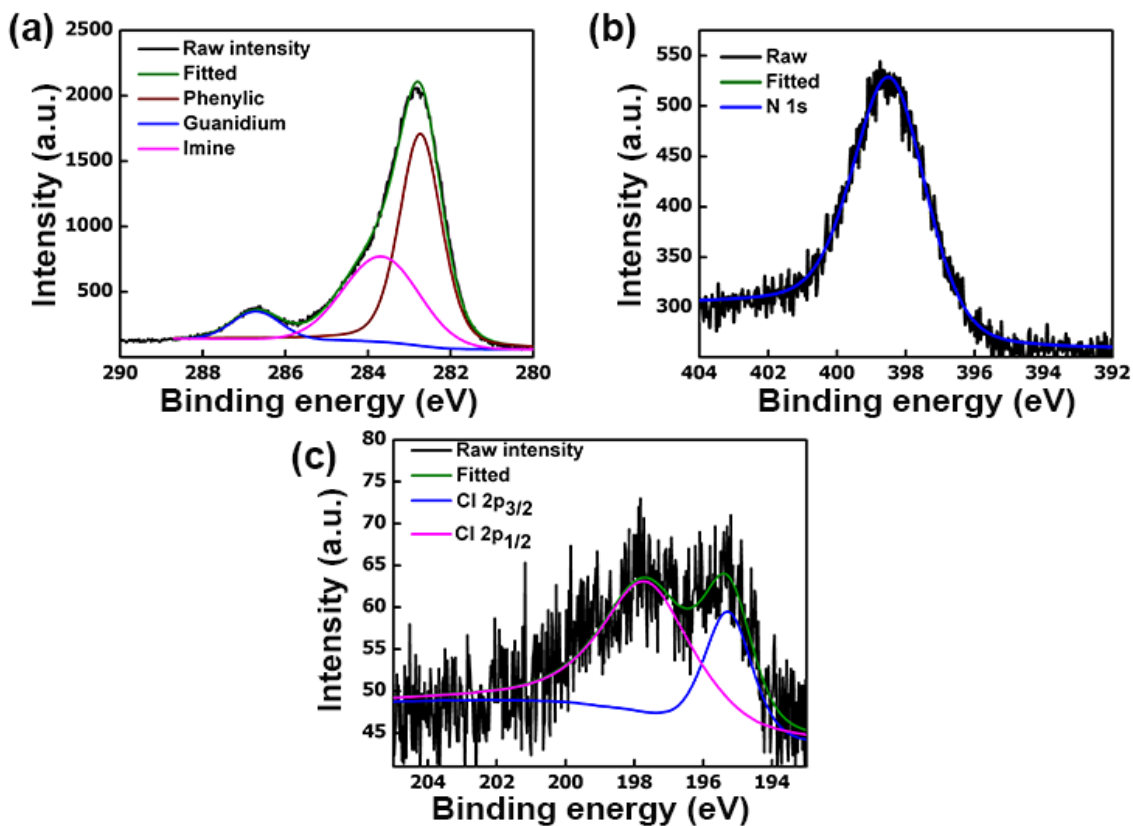


Fig. S19 The XPS analysis of POF1 for (a) C1s, (b) N1s, and (c) Cl2p, respectively.

## (f) Gas adsorption studies of POFs and Zn/POFs

### (i) Nitrogen gas sorption and porosity

The nitrogen sorption isotherms of POFs and Zn/POFs indicate type II isotherms (Fig. 1j, S20). The pore size distribution plots were estimated using the nonlocal density functional theory (NLDFT) method, confirming the hierarchical porosity from micro to mesoporous region (Fig. 1k). The specific BET surface area plots of POF2, as well as Zn/POF2, are shown in Fig. S21. The plot is obtained by fitting the BET equation given below.

$$\frac{P/P_0}{n \left(1 - \frac{P}{P_0}\right)} = \frac{1}{n_m C} + \frac{C - 1}{n_m C} (P/P_0)$$

Where  $P/P_0$  refers to the relative pressure,  $n_m$  refers to the specific monolayer capacity,  $n$  is the specific amount adsorbed at  $P/P_0$ , and  $C$  is the BET constant. The low value of the BET constant of Zn/POF2 ( $C = 10.8$ ) refers to the decrease in the micropore regime as compared to POF2 ( $C = 70.8$ ), which suggests the blocking of micropores through the impregnation of ZnO with the network.<sup>7</sup>

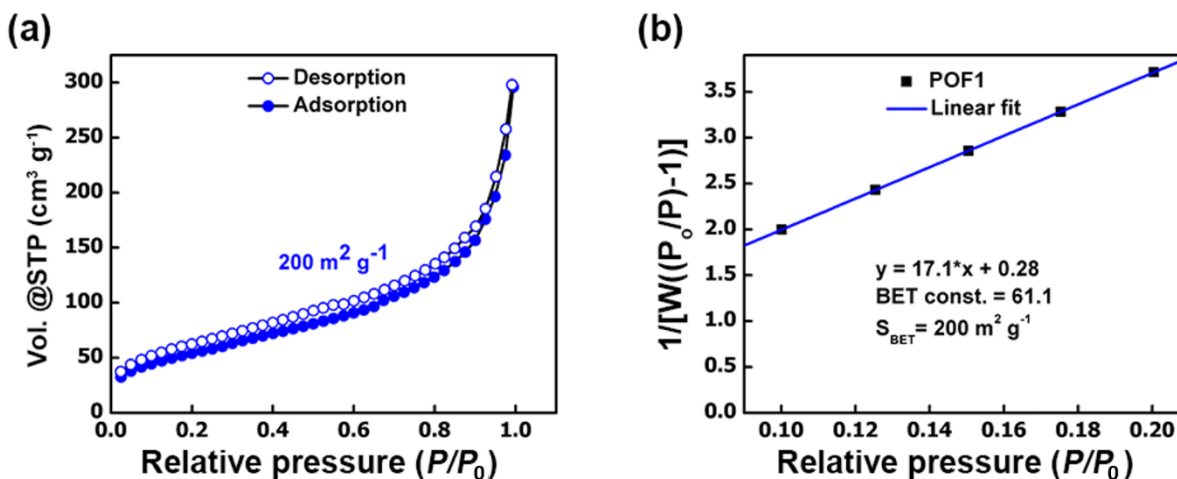
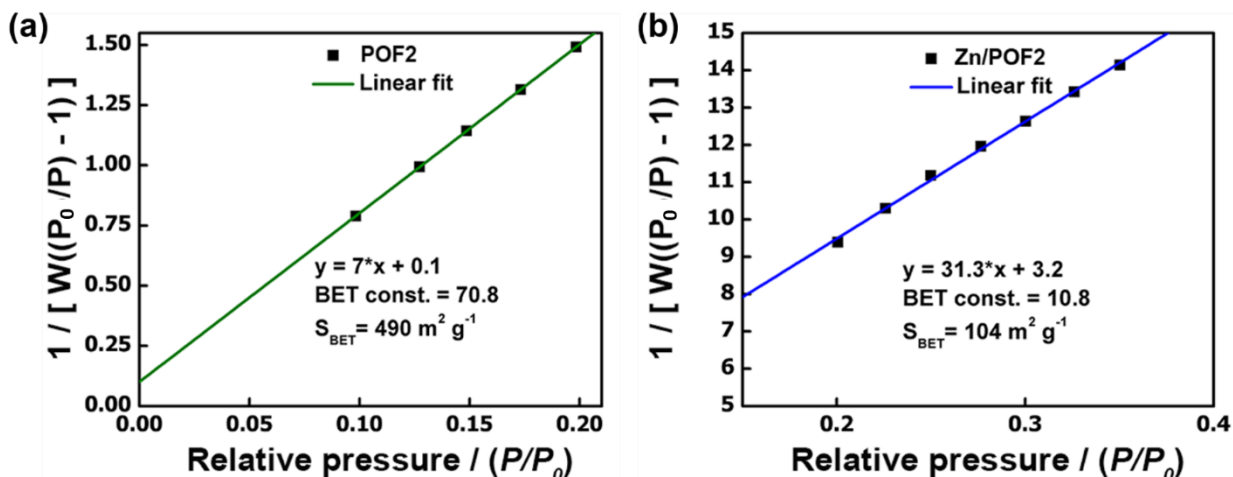


Fig. S20 (a) Nitrogen sorption profile of POF1 and (b) the specific BET surface area plot of POF1.



**Fig. S21** The specific BET surface area plot of (a) POF2 and (b) Zn/POF2.

### (ii) CO<sub>2</sub> sorption and selectivity

The CO<sub>2</sub> adsorption isotherms of POFs and Zn/POFs collected at 273 K along with the CO<sub>2</sub>/N<sub>2</sub> selectivity are shown in Fig. S22-S24. The CO<sub>2</sub> interaction with the POFs can be estimated by the enthalpy of adsorption (Fig. S25) following the Clausius-Clapeyron equation given below.<sup>7</sup>

$$\ln\left(\frac{P_1}{P_2}\right) = \frac{\Delta H_{ads}}{R} \left(\frac{1}{T_2} - \frac{1}{T_1}\right)$$

The CO<sub>2</sub>/N<sub>2</sub> selectivity was further evaluated by employing Ideal Adsorbed Solutions Theory (IAST) for the pure components.<sup>8</sup> A flue gas composition of 15% CO<sub>2</sub> and 85% N<sub>2</sub> was taken according to IAST for the calculation of selectivities.<sup>8</sup>

$$Selectivity, (S) = \frac{q_1/q_2}{p_1/p_2}$$

Where, q<sub>1</sub> and q<sub>2</sub> are the amount of adsorbate at pressure p<sub>1</sub> and p<sub>2</sub>, respectively. The hysteresis loops present in the CO<sub>2</sub> adsorption-desorption isotherms (Fig. S22a, S23a, S24a) of POFs and Zn/POFs indicate the flexibility of the network as well as the kinetic trapping of CO<sub>2</sub> inside the N-rich pores of the frameworks during the sorption experiment.<sup>9</sup>

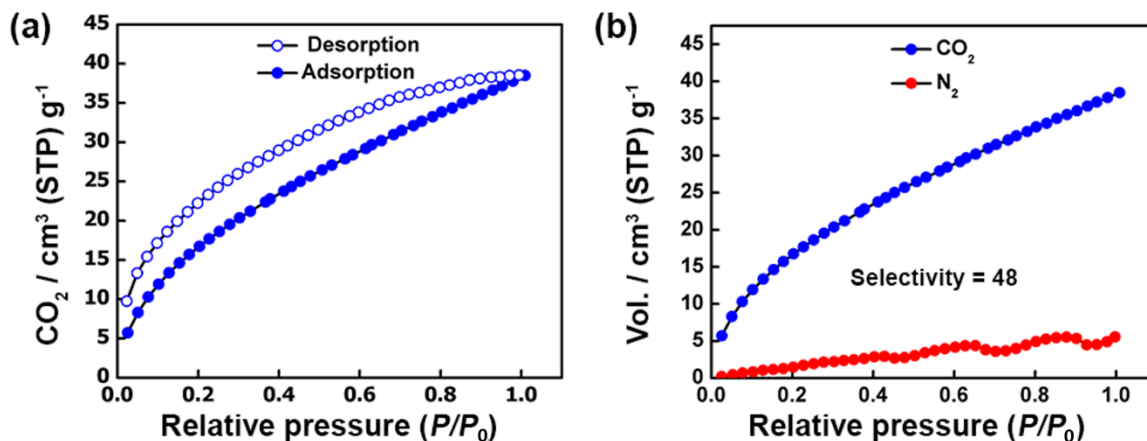


Fig. S22 (a) CO<sub>2</sub> sorption and (b) CO<sub>2</sub> over N<sub>2</sub> selectivity of POF2 measured at 273 K and 1 bar.

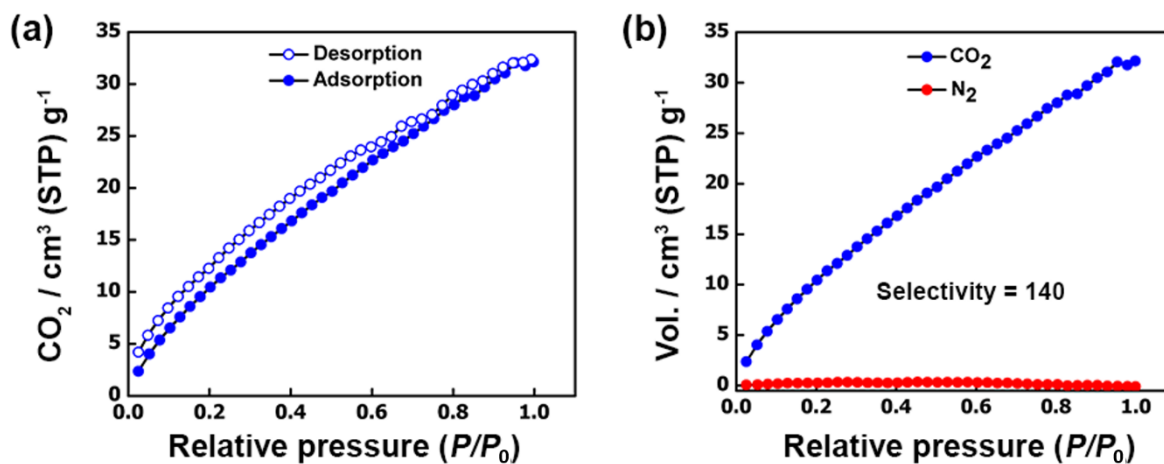


Fig. S23 (a) CO<sub>2</sub> sorption and (b) CO<sub>2</sub> over N<sub>2</sub> selectivity of POF1 measured at 273 K and 1 bar.

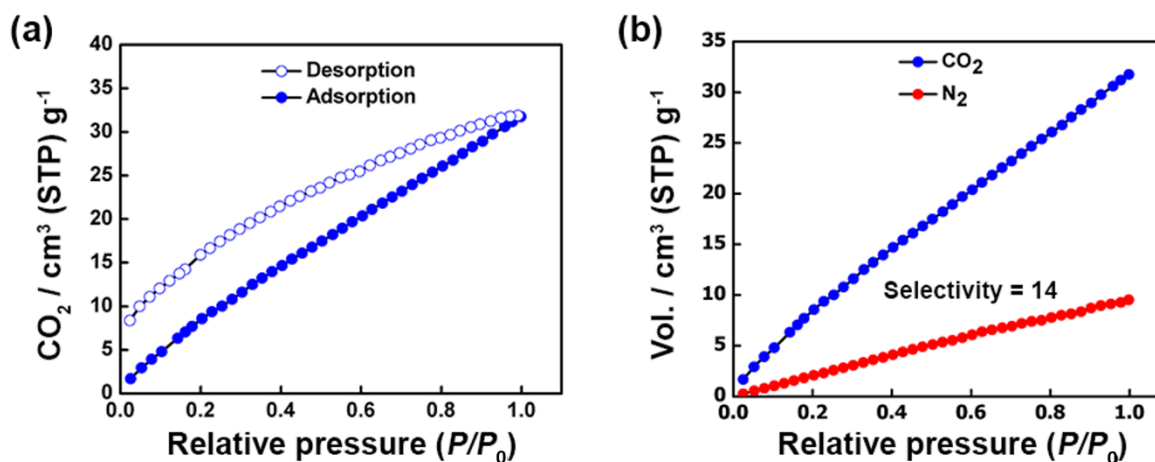
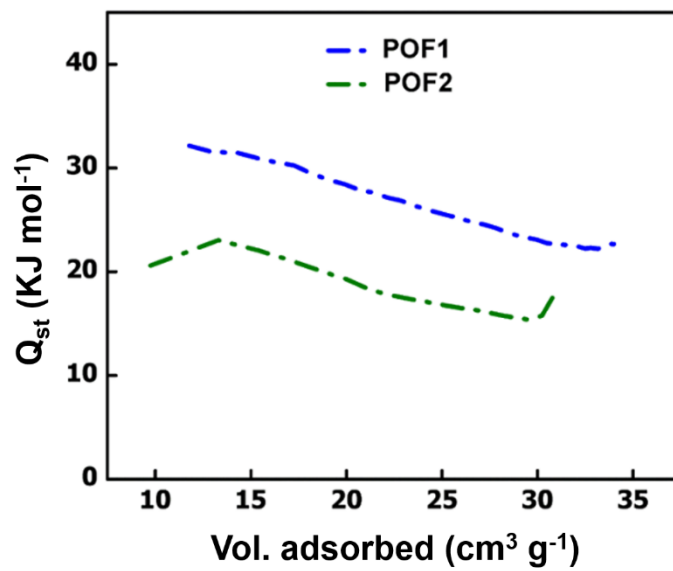


Fig. S24 (a) CO<sub>2</sub> sorption and (b) CO<sub>2</sub> over N<sub>2</sub> selectivity of Zn/POF2 measured at 273 K and 1 bar.



**Fig. S25** The  $\text{CO}_2$  isosteric heat of adsorption profiles of POF1 (blue) and POF2 (green).

## IV. CO<sub>2</sub> conversion catalyzed by POFs and Zn/POFs

All the CO<sub>2</sub> conversion experiments were performed with 17.2 mmol of the epoxide and a CO<sub>2</sub> pressure of 2.5 bar. Briefly, TBAB (2.5 mol%) and catalyst (POF or Zn/POF, 20 mg) were taken in a Schlenk-sealed tube and deaerated and filled with CO<sub>2</sub>. Under ice-cold conditions, epoxides of particular interest were added, and the CO<sub>2</sub> pressure was set at 2.5 bar and was further stirred at 90 °C. Then, the reaction mixture was allowed to cool, and 1,1,2,2-tetrachloroethane was added as an external NMR standard for the calculation of % of conversion (Table S3). The product formed was isolated by column chromatography using 20% EtOAc/hexane as eluent.

**Table S3** Catalytic conversion of propylene oxide to propylene carbonate.

S. No.	Substance	Pressure (bar)	Reaction time (h)	Conversion <sup>#</sup>
1.	TBAB	2.5	9	17%
2.	MTAG	2.5	9	28%
3.	POF1/POF2 <sup>*</sup>	2.5	9	< 2%
4.	POF1	2.5	9	51%
5.	POF2	2.5	9	42%
6.	Zn/POF1	2.5	9	94%
7.	Zn/POF2	2.5	2	40%
8.	Zn/POF2	2.5	6	85%
9.	Zn/POF2	2.5	9	92%
10.	ZnO bulk <sup>†,§</sup>	2.5	9	65%
11.	ZnO NPs <sup>§</sup>	2.5	9	86%

<sup>#</sup>% conversion calculated by the <sup>1</sup>H NMR using 1,1,2,2-tetrachloroethane as an external standard. The results were cross-verified by calculating the GC yields using the same external standard. <sup>\*</sup>In the absence of cocatalyst (TBAB). <sup>†</sup>The amount used is identical with ZnO present in Zn/POF2 (57 wt%), <sup>§</sup> nonrecyclable.

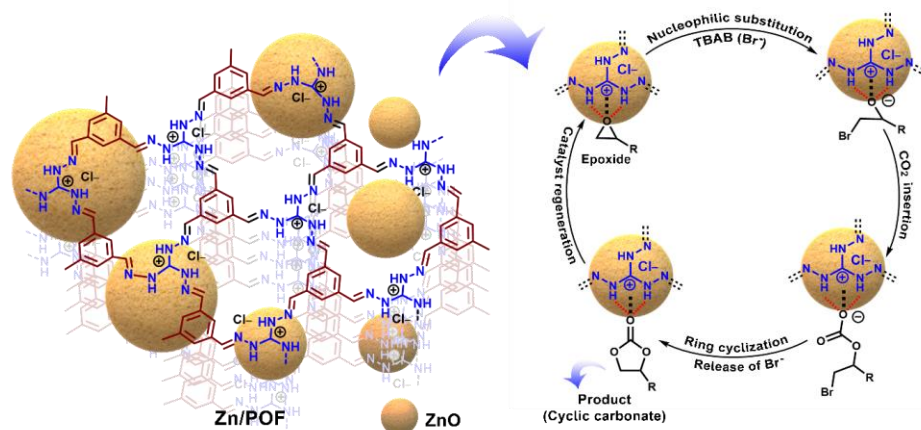


**Fig. S26** A plausible mechanism of CO<sub>2</sub> conversion depicting the synergistic effect of Lewis-acidic ZnO and –NH functionality present in the framework (crystallite/particle size of ZnO is not to scale as per the pore sizes of the frameworks in the pictorial depiction).



A decrease in the percentage of conversion of cyclic carbonate was observed in subsequent cycles (Fig. S27a). However, the systematic analysis revealed that the decrease in conversion was due to the loss of catalyst amount during the filtration and was not due to the diminished catalyst activity (Fig. 2b, 2c, S27b, S27c).

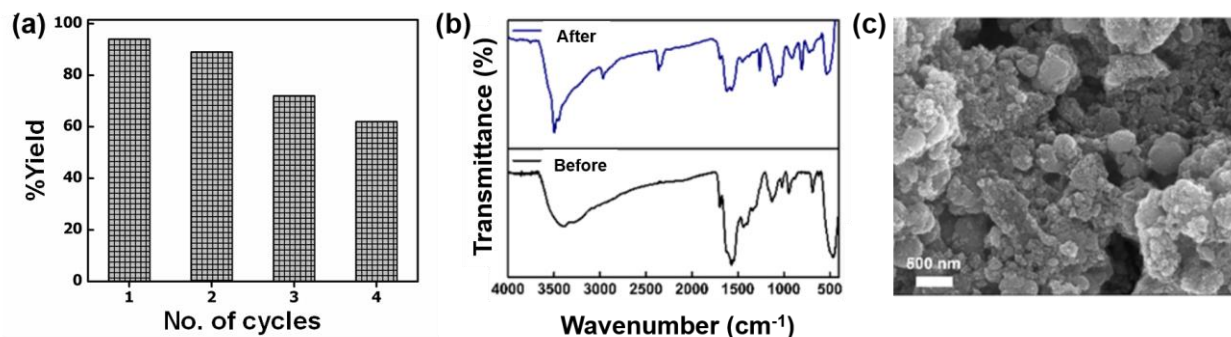


**Fig. S27** (a) The recyclability of Zn/POF2 after catalytic cycloaddition reaction between propylene oxide and CO<sub>2</sub>. However, if the catalyst amount is maintained (20 mg) circumventing the weight loss of 1-1.5 mg per cycle during the recovery process, more than 90% conversion for multiple cycles is ascertained (Fig. 2b). (b) FTIR spectra of the pristine and the regenerated catalyst (after 4<sup>th</sup> cycle) demonstrating the robustness of Zn/POF2 in catalytic CO<sub>2</sub> conversion. (c) The FESEM image depicting no change in the morphology of Zn/POF2 after four catalytic cycles in comparison with the pristine one (Fig. 1h).

We performed the control experiment with bulk ZnO for the catalytic conversion of epoxide (propylene oxide) into cyclic organic carbonates that showed ~ 65% conversion in the optimized reaction conditions (Fig. S49). We found with ZnO nanoparticles (size < 100 nm), ~85% conversion under identical conditions (Fig. S50). However, the catalyst was not recoverable after the reaction (from 20 mg catalyst, ~ 6 mg could be recovered: eventually, the catalytic conversion during the second cycle reduced to ~ 20%). The conversion of styrene oxide using ZnO nanoparticles was found to be 66% (Fig. S51). On the other hand, Zn/POFs showed excellent catalytic activity (92-99% conversion) with easy recyclability in identical reaction conditions. The high catalytic efficiency of Zn/POFs suggests the importance of N-rich CO<sub>2</sub>-philic ionic frameworks for the activation of epoxides in addition to the Lewis acidic metal centres (Fig. S26).

**Table S4** The quantitative analysis of metal leaching from Zn/POF2 through ICP-OES analysis.

S. No.	Name of the samples	Amount of Zn <sup>2+</sup> (wt%)
1.	Zn/POF2 (Before reaction)	49.98
2.	Zn/POF2 (After 4 <sup>th</sup> cycle)	47.97

## V. Antibacterial and antiviral studies with POFs and Zn/POFs

---

### Bacterial strains and culture conditions:

The Gram-positive *Staphylococcus aureus* (*S. aureus* ATCC® 6538P™) and Gram-negative *Escherichia coli* (*E. coli* ATCC® 8739™) were obtained from HiMedia Laboratories. Both the bacterial strains were grown in Luria-Bertani (LB) broth medium (DIFCO™ LB Broth, Miller, Lot-8079540). Both bacterial strains were cultured overnight, aerobically at 37 °C in a culture tube/flask with shaking at 200 rpm in a shaker incubator (INFORS HT, Ecotron). In order to investigate the antimicrobial activity of nanoporous frameworks, an estimation of bacterial growth was carried out using a spectrophotometer (Eppendorf, Germany) and the plating assay was performed as the measure of bacterial growth and viability.<sup>10</sup> All the measurements were performed with three replicates (n = 3), and the error bars represent standard deviation from the mean.

### (a) Antibacterial activity analysis:

We cultured both Gram-positive, and Gram-negative bacteria in LB supplemented with the nanoporous frameworks. Culture lacking nanoporous frameworks served as control and nanoporous frameworks containing media having no bacteria was taken as a blank control to eliminate the optical interference. The overnight grown culture was inoculated in the respective media for the experiment in a 12 well format at initial cell OD600 of 0.05-0.06 as measured in a

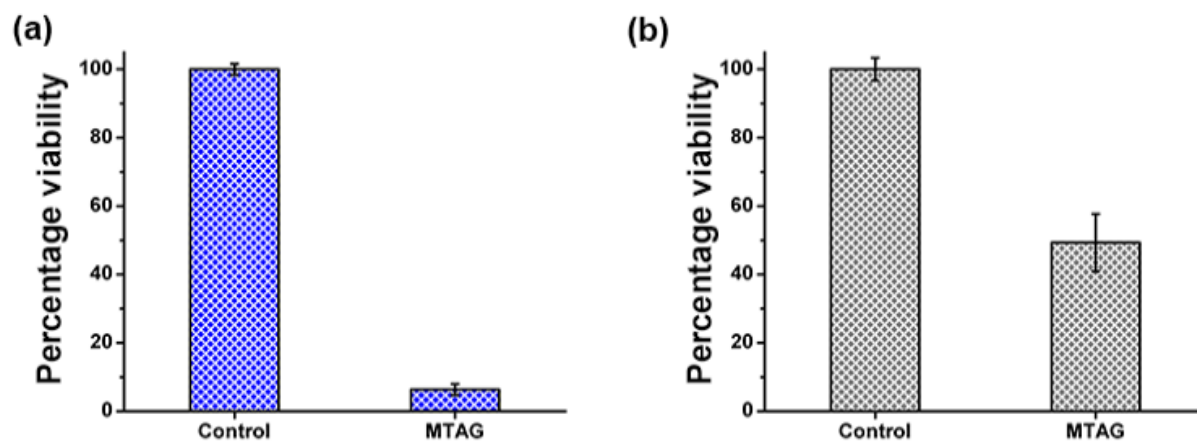


**Fig. S28** The antibacterial activity of the model compound of POF2 (MTAG, 500 µg/mL) against (a) Gram-positive bacteria (*Staphylococcus aureus*) and (b) Gram-negative bacteria (*Escherichia coli*) indicating the antibacterial activity of N-rich pristine ionic core.

spectrophotometer (Eppendorf, Germany). After incubating the culture for 12-15 h, the optical density (OD) was measured and diluted further (x1000) for LB agar plating.

**(i) Colony-forming unit (CFU) analysis:**

The CFU assay was used to deduce the antibacterial activity of the porous materials.<sup>11</sup> The bacterial suspensions containing various doses of POF2 or Zn/POF2 (100, 200, 500 µg/mL) were incubated for 12 h at 37 °C. The living cells were taken from the suspension, diluted 1000-fold, and were allowed to grow on agar plates overnight at 37 °C for the assessment of the colony-forming units (CFU). The suspension without POF2 or Zn/POF2 served as control. The images of the representative agar plates were captured using a DSLR D5300 camera.

**(ii) Growth curve analysis:**

The growth dynamics of the bacteria containing POF2 and Zn/POF2 were observed by using the diluted bacterial culture (OD 0.05) maintained in 24 well plate. Bacterial growth curves measurements were obtained in triplicates using plate reader SpectraMax i3X (Molecular Devices, USA). LB containing respective frameworks was taken as blank control. The bacterial suspension without porous frameworks was taken as control. Readings were captured in a span of 2 h in kinetics mode.

**(iii) TEM analysis of bacteria:**

For the TEM analysis, bacteria (both control and treated) were captured in the mid-log phase and then pellets of bacteria obtained by centrifugation (6000xg for 3 minutes) and washed with 0.1 M phosphate buffer solution (PBS). Afterwards, the pellets were fixed with 0.5 mL of 2.5 % glutaraldehyde solution for 20 minutes following a reported protocol,<sup>12</sup> and then were subjected to a series of alcohol dehydration process for 1 minute each (using 30%, 50%, 70% aq. EtOH solution) followed by 0.1 M PBS washing. Finally, the pellets were dispersed in 1 mL of absolute ethanol, and 10 µL sample was drop cast on the TEM grids.

**(iii) AlamarBlue cytotoxicity assay:**

The AlamarBlue (HiMedia TC235) assay was performed as per the reported protocol with a slight modification.<sup>13</sup> In this assay, a blue colored resazurin (nonfluorescent) dye gets converted to a pink colored resorufin (fluorescent) dye in the presence of live cells (Fig. S29-S30).

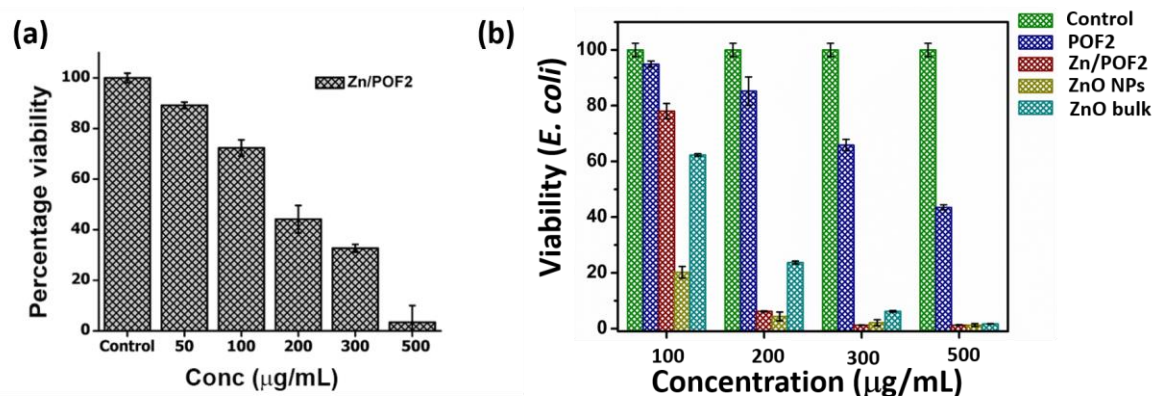


**Fig. S29** (a) The alamarBlue cell viability fluorescence-based assay for Gram-negative (*E. coli*) bacteria showing reduced fluorescence intensity indicating the decrease in the bacterial population with increasing the amount of Zn/POF2. (b) Comparative study against the Gram-negative bacteria (*E. coli*) showing percentage viability with increasing concentration of POF2, Zn/POF2, ZnO nanoparticles (NPs), and bulk ZnO powder.

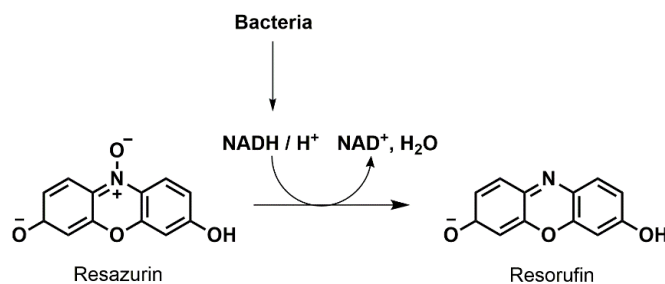


**Fig. S30** Schematic illustration of bacterial reduction mechanism of nonfluorescent resazurin to fluorescent resorufin in the alamarBlue-based assay.

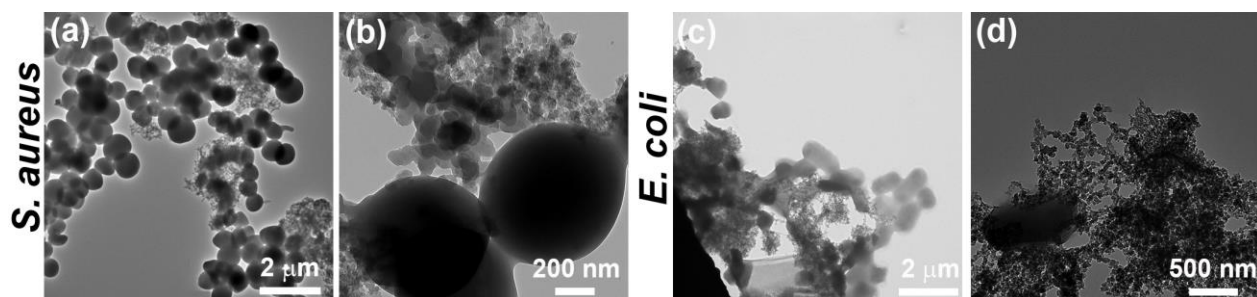


**Fig. S31** Analysis of cell integrity upon treatment of POF2 using transmission electron microscopy (TEM): (a, b) Gram-positive bacteria (*S. aureus*) and (c, d) Gram-negative bacteria (*E. coli*).

**(b) Bacterial biofilm formation:**

The bacterial biofilm formation assay was performed following a reported protocol.<sup>14</sup> Briefly, a single colony was maintained till the mid-log phase, and a 50  $\mu\text{L}$  of 100-fold diluted in LB medium culture was incubated aerobically in 96-well format for 24 h. The post incubated wells were washed with water several times to remove the unbounded bacteria. The wells were further stained with 0.1% crystal violet (Sigma Aldrich) and washed after 5 minutes of staining with water, and the plate was air-dried overnight. Further, the biofilm was treated for 2 h with POF2 and Zn/POF2. Post-treated biofilm was captured using a digital camera for visual assessment (Fig. S32) and further quantitatively by measuring absorbance at 570 nm by dissolving crystal violet in 33% acetic acid (Fig. 5a, 5b).

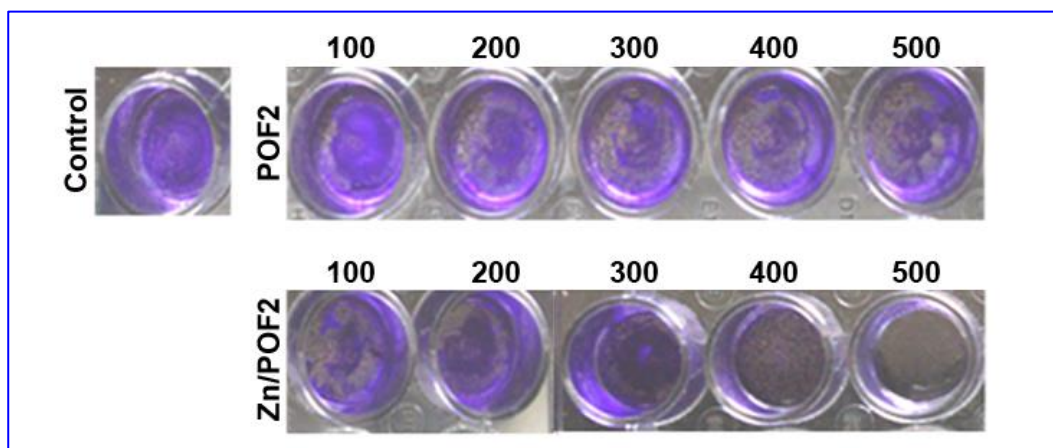


**Fig. S32** Bactericidal effects of POF2 and Zn/POF2 confirmed by their action on the biofilm disruption with increasing concentration ( $\mu\text{g}/\text{mL}$ ).

**(c) Antibacterial film coating:**

The antibacterial coatings employing Zn/POF2 were made using a 2% poly(vinylalcohol) in water solution. The effective concentration of Zn/POF2 was maintained as 500  $\mu\text{g}/\text{mL}$ , and the corresponding dispersion was coated on a glass slide using a spin coater. The coated slides were dried in an oven at 90  $^{\circ}\text{C}$  for 6 h before the antibacterial studies. The bacterial solution ( $\sim 10^5$  CFU/mL) was incubated in static conditions over the slide coated with Zn/POF2 in a Petri dish for 6, and 12 h at 37  $^{\circ}\text{C}$ . The bacterial growth was monitored by measuring OD at 600 nm (Fig. S33) and the percentage cell viability was plotted with respect to the control (only PVA coated slide).

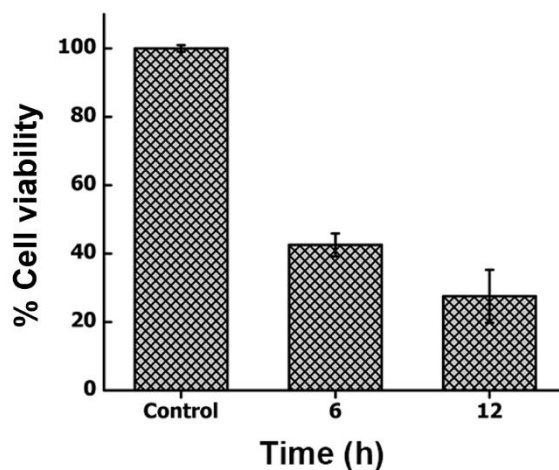


**Fig. S33** The antibacterial activity of PVA-Zn/POF2 thin film against Gram-negative bacteria (*E. coli*) at different timescale with respect to PVA film (control: the bacterial suspension overlaid on the PVA coated film, 12 h post-incubation, was considered as 100% viable population).

**(d) SYBR Green-I and propidium iodide (PI) staining:**

To determine the fraction of non-living cells against the living cells, the staining was performed with the nucleic acid stains like propidium iodide (PI) and SYBR Green-I.<sup>15</sup> The fluorophore stock solution of SYBR Green-I and PI were prepared following a standard protocol, filtered with 0.22  $\mu\text{M}$  membrane filters (Cole Parmer), and stored in the dark at  $-20$  and  $4$   $^{\circ}\text{C}$ , respectively.<sup>16</sup> A single colony of *E.coli* was inoculated and grown until the mid-log phase (the fastest bacterial growth phase, 7-8 h). The bacterial concentration was calculated by measuring optical density at 600 nm, and a bacterial stock of  $10^8$  CFU/mL was prepared by dissolving it in LB media. The Bacterial culture (2 mL) was mixed with the 500  $\mu\text{g}/\text{mL}$  of porous organic frameworks and maintained for 4 h at  $37$   $^{\circ}\text{C}$  in a continuous agitation in a shaker incubator. The cells were pelleted down and washed multiple times with the Hanks' balanced salt solution (HBSS) (Lonza, Switzerland) and finally resuspended in the same. Later, the cells were treated with 10x concentration of SYBR Green-I (Molecular Probes, Thermo Scientific, USA) and 2.5  $\mu\text{M}$  propidium iodide (Sigma Aldrich) solution in HBSS for 20 minutes. The post incubated cells were washed multiple times with HBSS, and 20  $\mu\text{L}$  resuspended cells were mounted on a glass slide with the help of ProLong<sup>TM</sup> Glass Antifade Mountant (Invitrogen, Thermo Scientific, USA) and kept for drying for 4 h. The fluorescent microscopic images were captured using a Zeiss Apotome fluorescence microscope (Carl Zeiss, Germany) using a 63x objective lens (Fig. 5c).

SYBR Green-I is a bacterial cell membrane permeable, nonspecific dye that can stain the live as well as the dead-cell. Whereas, propidium iodide (PI), the red-emitting fluorescent dye can only stain the dead cell. In the control bacterial cell (*E. coli*), the abundance of green fluorescence was found to be more than that of the red, suggesting the presence of a greater extent of the live cells. Whereas in both the POF2 and Zn/POF2 treated cells (*E. coli*), the abundance of red fluorescence was observed to a greater extent (indicative of dead cell population). The merged images depicting both red and green fluorescence (column 3, Fig. 5c) reflect the extent of the presence of live/dead cells. The study revealed that the cell membrane was intact (indicative of live population) as reflected by the green fluorescence signal from the SYBR Green-I in control (without porous frameworks). Whereas, the POF2 or Zn/POF2 treated cells showed a high red fluorescence due to possible rupture of the cell membrane and hence PI stained specifically the dead cell and SYBR Green-I penetrated nonspecifically to both the cells (live/dead) to result in a merged signal. Thus, it is confirmed that POF, as well as Zn/POF, rupture the bacterial cell membrane (Fig. 5c, S34).

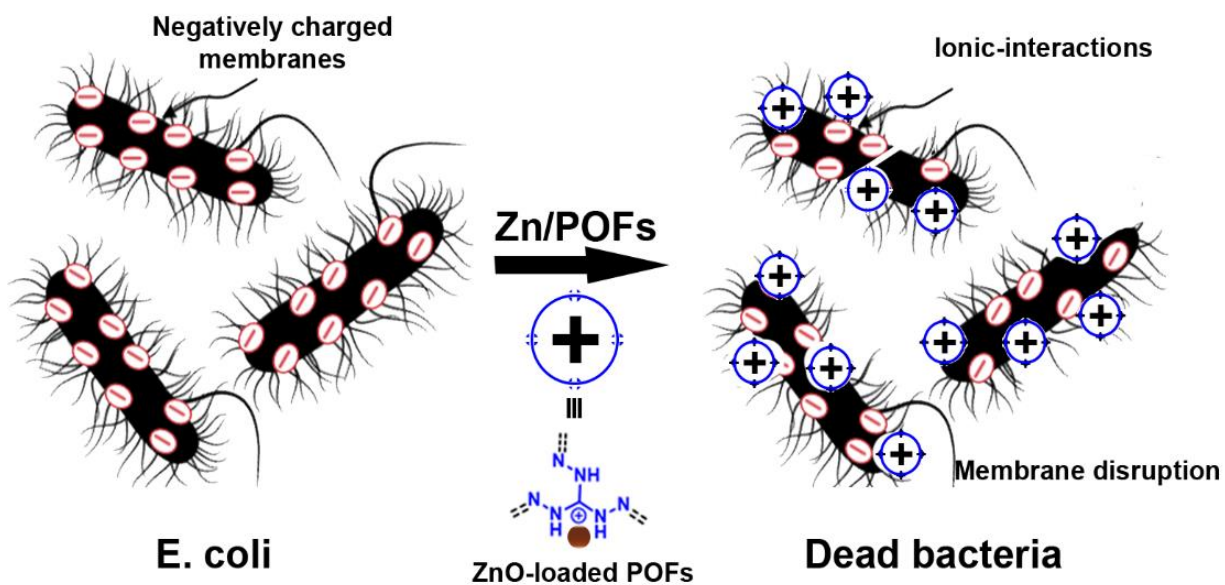


**Fig. S34** The mechanism of antibacterial activity of Zn/POFs against *Escherichia coli* (Gram-negative) bacteria (dimension of bacteria and ZnO-infused framework is not to scale in the pictorial depiction).

### (e) Water purification

The columns for the purification of water were prepared using a Pasteur pipette (Fig. S35). First, polystyrene beads of weight  $\sim 50$  mg were loaded into the Pasteur pipette for packing the thin neck followed by a cotton plug of equal weight ( $\sim 16$  mg) in control and the test column. The Zn/POF2 of  $\sim 50$  mg was loaded for the column-based purification of water. As a control, an equal amount of agarose was loaded, and the bacteria-contaminated water was allowed to pass through the packed column (flow rate:  $\sim 1$  mL/12 min without any external pressure, 0.5 cm column bed width). The bacteria-contaminated water was prepared by spiking a known concentration of *E. coli* ( $\sim 10^8$  CFU/mL) in ultra-pure water. The bactericidal effect of Zn/POF2 was examined by the CFU plating studies (Fig. S35), SYBR Green-I/ PI live/dead cell assay (Fig. S36), as well as the DNA leaching assay followed by agarose gel electrophoresis (Fig. S37).

A complementary experiment involving the analysis of released DNA from the Zn/POF2 column-treated water, as a function of bacterial lysis, was performed next. A 0.7 % agarose gel was made in 1x tris-acetate-EDTA (TAE) buffer. The DNA was visualized on the gel using the SYBR Safe-DNA gel stain (Invitrogen, Thermo Scientific). In order to compare the size of the DNA, the 1 KB plus DNA ladder (Fermentas) was used. The input contaminated water was heated

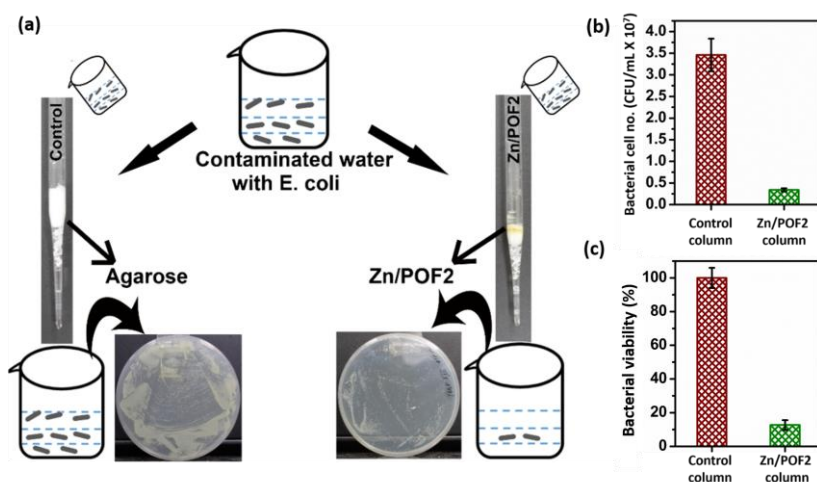


**Fig. S35** (a) The clearance of bacteria-contaminated water by passing through the columns packed with Zn/POF2 in comparison with the agarose-loaded column (control). Bacterial load after filtration was quantified by calculating (b) CFU/mL using agar plating method, and (c) percentage bacterial viability assessment (based on absorbance (OD) @ 600 nm). The bars represent the standard deviation from the mean ( $n = 3$ , mean  $\pm$  s.d).



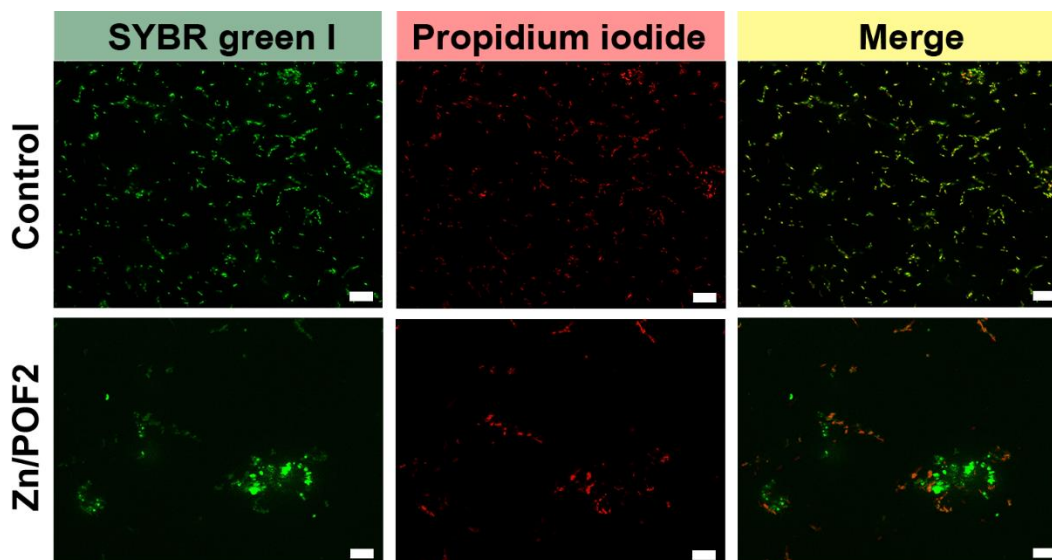


**Fig. S36** Live/dead bacterial cell imaging using a dye mixture of SYBR Green I and propidium iodide for staining the bacterial water sample (*E. coli*) after passing the column containing Zn/POF2. Column without Zn/POF2 is considered as control (scale bar = 5  $\mu$ m).

at 90 °C to get a positive control for lysis. The flow-through from the respective columns (20  $\mu$ L each) was mixed with 6x DNA loading dye and was loaded on the agarose gel for electrophoresis (Fig. S37). The presence of more DNA content on the agarose gel in the case of Zn/POF2 (lane 4, Fig. S37) as compared to the background (lane 3) indicated its high bactericidal activity.

**(f) Bradford assay:**

Further to validate bacterial lysis, we performed Bradford protein quantification assay on the filtered water following a standard protocol.<sup>17</sup> Precisely, 100  $\mu$ L of filtrate after centrifugation

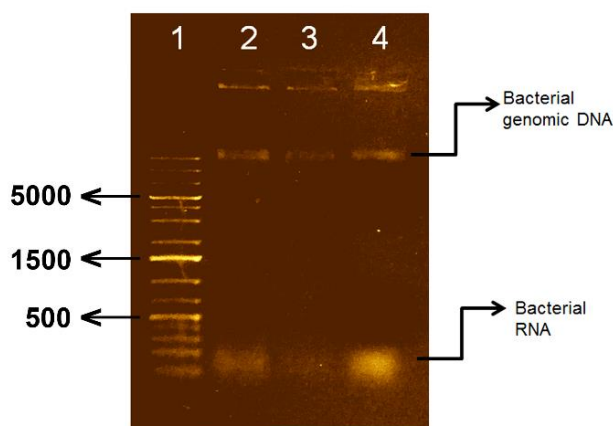


**Fig. S37** Agarose gel electrophoresis for the eluted water sample. Lane 1: DNA ladder, lane 2: positive control lysate, lane 3: elution from agarose packed column, lane 4: elution from Zn/POF2 packed column.

(removal of live bacteria) was mixed with 3 mL of Bradford reagent (Sigma Aldrich) in a glass tube and was incubated for five minutes at room temperature. Post-incubation, 200  $\mu$ L of the reaction mixture in triplicates was transferred into 96 well plate, and the absorbance was measured at 595 nm. Bradford reagent having no filtrate was used as blank. The high value of absorbance (presence of more protein) obtained in flow-through from the Zn/POF2-packed column as compared to the agarose-packed column is indicative of more lysis-associated intracellular protein release. Data was represented as bar plot (Fig. 5e).

### **Antiviral activity**

**Cell lines:** The TZM-GFP and HEK293T cell lines described previously,<sup>18</sup> were maintained in Dulbecco's Modified Eagle Medium with L-glutamine containing 10% heat-inactivated fetal bovine serum (FBS) (Gibco, Thermo Scientific USA, Cat. No. 10082147, lot no. 2097440). The cells were incubated at 37°C in a humidified 5% CO<sub>2</sub> incubator (NuAire, USA). Cell monolayers were maintained at a split ratio of 1:10 by treatment with 0.25% trypsin, 1 mM EDTA (Invitrogen, Thermo Scientific, USA). All the measurements were performed with four replicates (n = 4), and the error bars represent standard deviation from the mean.

### **(g) Virus production:**

A replication-defective single cycle NL4-3 (carrying a defect in Env and Nef open reading frame) was trans-complemented with HXB2 envelope coding plasmids, and was co-transfected in HEK293T cells using a calcium phosphate method.<sup>18</sup> The virus-containing culture supernatants were collected after 48 h of transfection, clarified by centrifugation at 300xg for about 5 minutes, and passed through filters of 0.45- $\mu$ m pores (Cole-Parmer) as described previously.<sup>19</sup> For lentiviral pseudoparticles generation, we used ZS-Green reporter expressed through pScalps,<sup>20</sup> psPAX2 (Addgene#12260), and pMD2.G (Addgene#12259, kind gift from Didier Trono), and were cotransfected in HEK293T cells using calcium phosphate method. Subsequent steps were the same as described for the HIV-1 virus.

### **(i) Virus quantification:**

The quantification of retroviral reverse transcriptase (RT) activity in retrovirus containing filtered supernatant by quantitative reverse transcription polymerase chain reaction (qRT-PCR) as a method for the titration of lentiviral/retrovirus vector was followed.<sup>21</sup>

**(ii) Infectivity assay:**

The virus was five-fold diluted in a series of four steps while adding in target cells (TZM-GFP). The TZM-GFP cells (seeded one day before infection) were infected for 48 h in 96 well format (Eppendorf, Germany).<sup>19</sup> Further, the infectivity was assayed as a function of green cells scored using CellInsight CX7 High-Content Screening (HCS) Platform (Thermo Fisher Scientific, USA) after counter staining the nuclei of total cells using Hoechst 33258 (Sigma Aldrich). The percentage of infectivity was represented (Fig. 6a, 6b). The representative images were captured using both CellInsight CX7 High-Content Screening (HCS) Platform (Fig. 6g) and SpectraMax i3x multimode microplate (Molecular Devices, USA) reader as shown in Fig. S38.

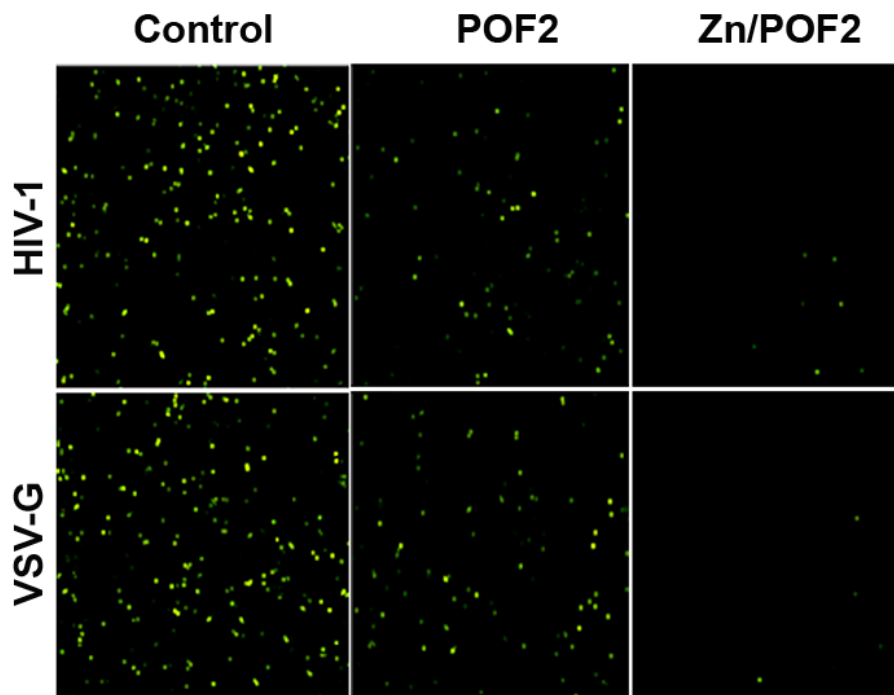


**Fig. S38** The fluorescence microscopy images of the single-cycle HIV-1 (top panel) and VSV-G psuedotyped lentiviral vector (bottom panel) infectivity against both POF2 and Zn/POF2 with respect to the control.

**(iii) Virus fusion assay:**

We employed the nlsCre delivery assay in order to evaluate the fusion of viruses in the target cells.<sup>18</sup> The Cre delivery upon virus fusion activates the RFP in the TZM lox RFP target cells. For this assay, virus production was carried out using p8.9 Cre and pMD2.G (Addgene plasmid #12259) in HEK293T cells. Virus was subsequently quantified as described earlier, diluted and added to the TZM lox RFP cells seeded one day before in 96 well format in the absence and

presence of porous frameworks (20  $\mu\text{g}/\text{mL}$ ). After 48 h of incubation, the red cells were scored and imaged using CellInsight CX7 High-Content Screening (HCS) Platform (Fig. 6c, 6d).

### (h) Cytotoxicity analysis using cell counting and alamarBlue assay:

In order to analyze the cytotoxicity associated with the porous frameworks along with a comparative analysis using ZnO and ZnO nanoparticles, we performed total cell counting assay by nuclear staining using Hoechst 33258 (Sigma-Aldrich).<sup>22</sup> We incubated porous frameworks with TZM-GFP target cell lines for 48 h. Post-incubation, cells were fixed using 4% paraformaldehyde (Sigma-Aldrich) and washed thrice with 1x PBS (Amresco), reconstituted using PBS tablets in Milli-Q water. Finally, cells were stained using Hoechst for 15 minutes at room temperature. Further, the staining was terminated by transferring the plate at 4  $^{\circ}\text{C}$ . Later, the cells were imaged and counted using CellInsight CX7 High-Content Screening (HCS) Platform (Thermo Fisher Scientific). The cell number represented in bar plots is shown in Fig. S39.

To check the cytotoxicity associated with the porous frameworks (POFs and Zn/POFs) in the host cells, firstly, TZM-GFP cells were incubated with the various doses of porous frameworks for 48 h.<sup>18</sup> Post incubation, 1x alamarBlue (diluted from the 100x stock solution, i.e., 0.5 g in 100 mL 1x PBS) was added to the respective wells, and the fluorescence was recorded using SpectraMax i3x multimode plate reader (Molecular Devices, USA) and the corresponding bar plots showing cell viability were represented.<sup>13</sup>

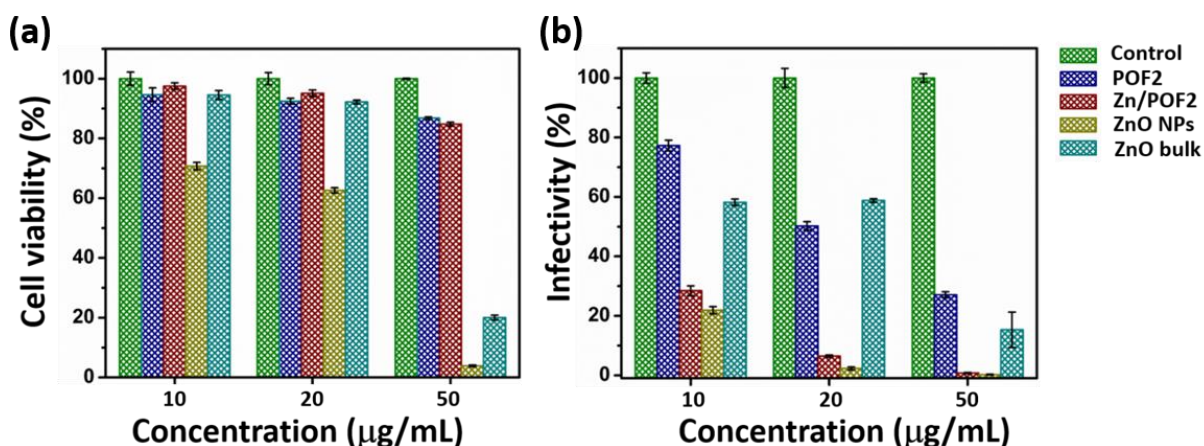


**Fig. S39** Comparative study of POF2, Zn/POF2 with ZnO nanoparticles (NPs), as well as bulk ZnO with varying doses showing (a) target cell viability (TZM-GFP) analysis, and (b) infectivity analysis using HIV-1.

Cell counting based cell viability assay (Hoechst based nuclear staining) indicates that the ZnO nanoparticles are toxic to the human cells in comparison to Zn/POF2, as shown in Fig. S39a. On the other hand, the antiviral activity of Zn/POF2 (20  $\mu\text{g}/\text{mL}$ ) is better than that of the bulk ZnO powder and comparable to the ZnO nanoparticles. In fact, the antimicrobial activity of pristine ZnO nanoparticles is further contributed by the cytotoxicity associated with ZnO nanoparticles (Fig. S39b). These data clearly ascertain that the developed materials are highly effective against the microbes with minimal cytotoxicity to the human cells.

**(i) Virus lysis assay:**

Virus particles containing supernatant were incubated for 2 h with the various doses of porous frameworks (5, 10, 20  $\mu\text{g}/\text{mL}$ ). After incubation, frameworks were removed using centrifugation at 500xg and 5  $\mu\text{L}$  supernatants were taken to quantify the virus particles using SG-PERT assay with the SG-PERT lysis buffer as a control for effective lysis. The frameworks lyse the viruses and release the reverse transcriptase (RT) from the viral core, as reflected in the SG-PERT assay (Fig. 6e, 6f, S40).

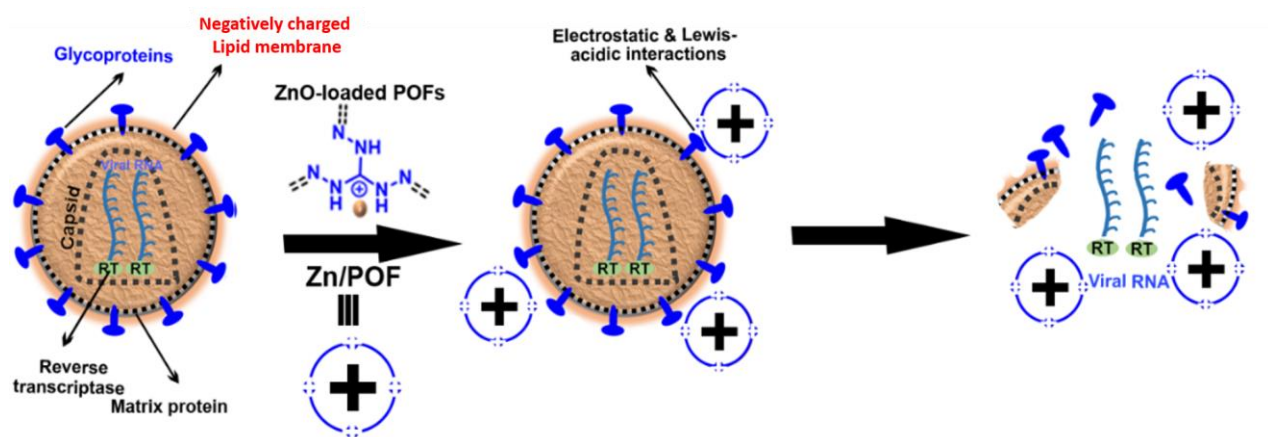


**Fig. S40** The plausible mechanism of antiviral activity of Zn/POFs against HIV.

## VI. Comparative tables

We studied the reports of some of the well-known composite materials where the metal loading was found to be significantly high (Table S5). The metal loading was highlighted as a key feature of the composite materials for the enhanced performance in some of the said applications, as listed below.

**Table S5** Comparative accounts of metal/metal oxide loading capacities (wt%) of triaminoguanidinium based porous ionic frameworks developed in the present study with other representative porous materials, like porous organic polymers (POPs), covalent organic frameworks (COFs), porous carbons (PCs), and metal organic frameworks (MOFs) for catalysis and biomedical applications.

Material	Metal loading <sup>#</sup>	Application	Reference
Zn/POF2	ZnO (57.3 ± 1.2 wt%); Zn (47.2 wt%)	CO <sub>2</sub> conversion to cyclic carbonates, antibacterial (biofilm disruption, water treatment) and antiviral agent	<i>Present work</i>
<b><i>Porous Organic Polymers (POPs)</i></b>			
HAzo-POP-1	Cu (26.2 wt%), Zn (23.5 wt%), Ni (20.6 wt%)	CO <sub>2</sub> conversion to cyclic organic carbonates, oxidation of benzyl alcohols	<i>Angew. Chem. Int. Ed.</i> , 2016, <b>55</b> , 9685. <sup>23</sup>
PAF-50	Ag (39.9 wt%)	Antibacterial polymer coatings	<i>Adv. Mater.</i> , 2013, <b>25</b> , 6619. <sup>24</sup>
Co-CMP Al-CMP	Co (7.3 wt%), Al (3.5 wt%)	CO <sub>2</sub> conversion to cyclic organic carbonates	<i>Nat. Commun.</i> , 2013, <b>4</b> , 1960. <sup>25</sup>
PPh <sub>3</sub> - ILBr-ZnBr <sub>2</sub> @POPs	Zn (4.6 wt%)	Conversion of CO <sub>2</sub> to cyclic carbonates	<i>ACS Catal.</i> , 2016, <b>6</b> , 6091. <sup>26</sup>
Poly-(PPh <sub>3</sub> )-azo-Ag, Poly-(PPh <sub>3</sub> )-azo-Ru	Ag (0.2 wt%) Ru (3.7 wt%)	Carboxylative cyclization of propargyl alcohol with CO <sub>2</sub>	<i>ACS Catal.</i> , 2016, <b>6</b> , 1268. <sup>27</sup>
POPs Bp-Zn@MA	Zn (1.9 wt%)	Synthesis of cyclic carbonates from flue gas	<i>Green Chem.</i> , 2016, <b>18</b> , 6493. <sup>28</sup>
Ag-SN1-CMP	Ag (12.3 wt%)	Effective antimicrobial carriers	<i>ACS Appl. Bio Mater.</i> , 2018, <b>1</b> , 473. <sup>29</sup>
<b><i>Covalent Organic Frameworks (COFs)</i></b>			
Pd/COF-LZU1	Pd (7.1 ± 0.5 wt%)	Suzuki–Miyaura coupling reaction	<i>J. Am. Chem. Soc.</i> , 2011, <b>133</b> , 19816. <sup>30</sup>
PdNPs@COF PtNPs@COF	Pd (26.3 wt %) Pt (34.4 wt %)	Nitrophenol reduction and Suzuki–Miyaura coupling reaction	<i>J. Am. Chem. Soc.</i> , 2017, <b>139</b> , 17082. <sup>31</sup>
Cu@COF	Cu (7.0 wt%)	Synthesis of unsymmetrical diynes via Glaser–Hay coupling	<i>ACS Appl. Mater. Interfaces</i> , 2019, <b>11</b> , 15670. <sup>32</sup>

COF-Co/Co(OH) <sub>2</sub>	Co (16.0 wt%)	Hydrogen evolution and one-pot organic reductions	<i>Small</i> , 2018, <b>14</b> , 1801233. <sup>33</sup>
<b><i>Porous Carbons (PCs)</i></b>			
ZnO@polymer ZnO@carbon	Zn (10.9 wt%), (1.5 wt%)	Selective hydrogenation of phenylacetylene to phenylethylene	<i>Adv. Funct. Mater.</i> , 2018, <b>28</b> , 1801737. <sup>34</sup>
ZnO@NC/S-1(0.0) ZnO@NC/S-1(1.0)	Zn (2.8 wt%) (2.0 wt%)	Propane dehydrogenation	<i>iScience</i> , 2019, <b>13</b> , 269. <sup>35</sup>
<b><i>Metal Organic Frameworks (MOFs)</i></b>			
Cu@MOF-5 Pd@MOF-5 Au@MOF-5	Cu (13.8 wt%) Pd (35.6 wt%) Au (48.0 wt%)	Methanol synthesis	<i>Angew. Chem. Int. Ed.</i> , 2005, <b>44</b> , 6237. <sup>36</sup>
Cu@MOF-5 Cu/ZnO@MOF-5	Cu (11.2 wt%) Zn (47.6 wt%)	Methanol synthesis	<i>Chem. Mater.</i> , 2008, <b>20</b> , 4576. <sup>37</sup>
Cu-Pd@MIL-101	Cu-Pd (10.4 wt%)	Homocoupling reaction of phenylacetylene	<i>ACS Cent. Sci.</i> , 2019, <b>5</b> , 176. <sup>38</sup>
<b><i>Porous Silica Composite</i></b>			
3c-ZnO/SiO <sub>2</sub>	ZnO (45.1 wt%)	Atomic layer deposition of ZnO on mesoporous silica	<i>Nanomaterials</i> , 2020, <b>10</b> , 981. <sup>5c</sup>

<sup>#</sup>Determined by TGA, ICP-OES, ICP-MS, XRF, or elemental analysis.

**Table S6:** A comparative account of CO<sub>2</sub> conversion to cyclic organic carbonates by POFs and Zn/POFs in comparison with the other reported catalysts including homogeneous catalysts, inorganic catalysts, MOFs, ionic liquids, cage compounds, porous silica-based materials, metal loaded frameworks (M-POFs), and porous organic polymers.

S. No.	Substance	Pressure (bar)	Temp. (°C)	TBAB	Conversion (%), <sup>#</sup> time (h)	Reference
1.	Zn/POF1	2.5	90	2.5 mol%	94 (9)	<i>Present work</i>
	Zn/POF2				99 (9) <sup>\$</sup>	
					92 (9)	
<b>Homogeneous catalysts</b> (Solvent-mediated catalysis, post-synthetic purification needed, entry 2, 3: inorganic catalysts)						
2.	Al-catalyst C*	10	25	5 mol%	99 (14)	<i>Angew. Chem. Int. Ed.</i> , 2016, <b>55</b> , 3972. <sup>39</sup>
3.	Co(salen) (3g)*	1	25	Phosphorane	97 (36)	<i>Green Chem.</i> , 2017, <b>19</b> , 3908. <sup>40</sup>
4.	Squaramide-5*	10	45	5 mol% (TBAI)	74 (18)	<i>ACS Catal.</i> 2017, <b>7</b> , 3532. <sup>41</sup>
<b>Metal organic frameworks (MOFs)</b>						
5.	ZIF-8/CN	10	80	-	99 (24) <sup>\$</sup>	<i>Adv. Funct. Mater.</i> , 2017, <b>27</b> , 1700706. <sup>42</sup>
6.	Acrylamide-containing MOF	1	RT	0.5 g	96 (48)	<i>Chem. Mater.</i> , 2017, <b>29</b> , 9256. <sup>43</sup>
7.	Zn-DPA	10	100	0.3 mmol	99 (2)	<i>Nat. Commun.</i> , 2019, <b>10</b> , 4362. <sup>44</sup>
8.	Zn(II) organic framework with a Zn <sub>4</sub> (-COO) <sub>6</sub> cluster	1 atm	30-40	1 mol%	99 (24)	<i>Chem. Eur. J.</i> 2020, <b>26</b> , 788. <sup>45</sup>
<b>Ionic liquids</b>						
9.	PDmBr (ionic liquid)	10	110	-	99 (4)	<i>Chem. Sci.</i> , 2015, <b>6</b> , 6916. <sup>46</sup>
10.	KCC-1/IL/HPW NPs	10	90	-	98 (1.5)	<i>Green Chem.</i> , 2015, <b>17</b> , 3059. <sup>47</sup>
<b>Cage Compounds</b>						
11.	Co(III)@cage	1	25	10 mol%	$\frac{58 (48)}{99 (24 \text{ h})^{\$}}$	<i>Chem. Sci.</i> , 2019, <b>10</b> , 1549. <sup>48</sup>
12.	Cg-Am*	2.5	90	2.5 mol%	95 (9)	<i>Sustainable Energy Fuels</i> , 2019, <b>3</b> , 2567. <sup>49</sup>
<b>Porous Silica / Si-based materials</b>						
13.	I-POSS1a (Silsesquioxane)	7.5	110	-	88 (6)	<i>ACS Appl. Mater. Interfaces</i> , 2017, <b>9</b> , 3616. <sup>50</sup>



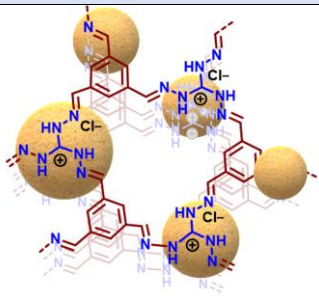
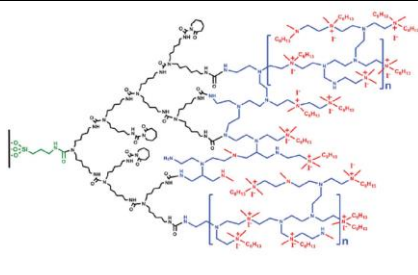
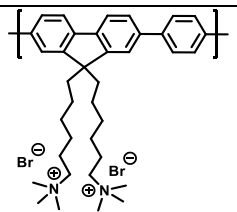
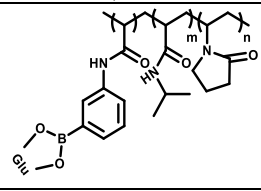
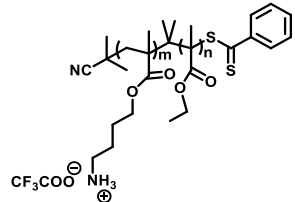
14.	0.2 EmimBr@mSiO <sub>2</sub>	20	120	-	87 (3)	<i>Green Chem.</i> , 2018, <b>20</b> , 3232. <sup>51</sup>
15.	Supported POSS based material (5b)	40	150	-	55 (3)	<i>ChemCatChem</i> , 2019, <b>11</b> , 560. <sup>52</sup>
<b>Metal loaded porous organic frameworks (M-POFs)</b>						
16.	Co-CMP	30	100	1.8 mol%	98 (1)	<i>Nat. Commun.</i> , 2013, <b>4</b> , 1960. <sup>53</sup>
17.	Zn(OAc) <sub>2</sub> loaded o- hydroxyazo POPs	30	100	7.2 mol%	90 (0.8)	<i>Angew. Chem. Int. Ed.</i> , 2016, <b>55</b> , 9685. <sup>23</sup>
18.	Co/Zn R@HMTA	10	100	7.2 mol%	99 (1.5)	<i>Adv. Mater.</i> , 2017, <b>29</b> , 1700445. <sup>54</sup>
19.	Zn/RN4-Az-OH	1	35	0.25 mmol	92 (24) <sup>§</sup>	<i>Chem. Mater.</i> , 2019, <b>31</b> , 8440. <sup>55</sup>
<b>Porous organic frameworks (POFs)</b>						
20.	N-Heterocyclic carbenes polymers	1	120	10 mol%	98 (24)	<i>Chem. Mater.</i> , 2015, <b>27</b> , 6818. <sup>56</sup>
21.	Porphyrin-based POPs	15	100	1 mol%	99 (5)	<i>Green Chem.</i> , 2018, <b>20</b> , 903. <sup>57</sup>
22.	COP-222	1	100	-	99 (24)	<i>Chem</i> , 2019, <b>5</b> , 3232. <sup>58</sup>
23.	N-rich click-based POP (CPP)	1	100	-	99 (24)	<i>ChemSusChem</i> , 2020, <b>13</b> , 180. <sup>59</sup>
<sup>#</sup> Propylene oxide or styrene oxide used as the substrate, unless stated otherwise; *Nonrecyclable <sup>§</sup> Epichlorohydrin used as substrate, catalysis further assisted by the anchimeric assistance of -Cl group						

Most of the catalysts required drastic reaction conditions ( $\geq 10$  bar of CO<sub>2</sub> pressure with 100-120 °C temperature) or otherwise milder conditions with longer reaction time (24 to 48 h). We could achieve 90-99% conversion for a range of substituted epoxides with milder reaction conditions (2.5 bar of CO<sub>2</sub> pressure at 90 °C) and reasonably lesser reaction time (9 h). However, we must emphasize that the catalytic conversion of CO<sub>2</sub> and epoxides into cyclic carbonates can certainly be improved further. Currently, the focus is to achieve the catalytic conversion at ambient conditions (1 atm, room temperature) in a shorter time. To the best of our knowledge, Zn/POFs hold a prominent place among the porous materials-based recyclable, heterogeneous catalysts for the conversion of a range of epoxides and CO<sub>2</sub> into cyclic carbonates. In this context, we also refer to a recent review article on imidazolium-functionalized organic cationic polymers for the conversion of CO<sub>2</sub> into cyclic carbonates justifying the ingenuity in our report.<sup>60</sup>

**Table S7** Comparison of multifunctional applications, including CO<sub>2</sub> conversion, antibacterial, and antiviral activities of POF2 and Zn/POF2 with some of the representative porous materials.

S. No.	Adsorbent	S <sub>BET</sub> (m <sup>2</sup> g <sup>-1</sup> )	CO <sub>2</sub> conv.	Antibacterial		Antiviral (HIV-1, VSV)	Reference
				<i>S. aureus</i>	<i>E. coli</i>		
1.	POF2	490	✓	✓	✓	✓	<i>Present work</i>
	Zn/POF2	104	✓	✓	✓	✓	
2.	PZP-nanocompo sites	-	-	✓	-	-	<i>Adv. Mater. Interfaces</i> , 2018, <b>5</b> , 1800167. <sup>61</sup>
3.	TpTG <sub>Br</sub>	305	-	✓	✓	-	<i>J. Am. Chem. Soc.</i> , 2016, <b>138</b> , 2823. <sup>2</sup>
	TpTG <sub>Cl</sub>	267	-	✓	✓	-	
4.	MOF-525/PCL MMMs	-	-	-	✓	-	<i>ACS Appl. Mater. Interfaces</i> , 2017, <b>9</b> , 41512. <sup>62</sup>
5.	ZIF-8/GO	-	-	-	✓	-	<i>ACS Appl. Mater. Interfaces</i> , 2016, <b>8</b> , 25508. <sup>63</sup>
6.	SURGEL	-	-	-	✓	-	<i>ACS Appl. Mater. Interfaces</i> , 2018, <b>10</b> , 1528. <sup>64</sup>
7.	PAF-50	384	-	✓	-	-	<i>Adv. Mater.</i> , 2013, <b>25</b> , 6619. <sup>24</sup>
	AgCl-PAF-50	-	-	✓	-	-	
8.	AgNPs-HNTs-rGO	-	-	✓	-	-	<i>J. Mater. Chem. A</i> , 2015, <b>3</b> , 18696. <sup>65</sup>
9.	PDMBr (ionic liquid)	-	✓	-	-	-	<i>Chem. Sci.</i> 2015, <b>6</b> , 6916. <sup>46</sup>
10.	cCTF-500	1247	✓	-	-	-	<i>ACS Appl. Mater. Interfaces</i> , 2017, <b>9</b> , 7209. <sup>66</sup>
11.	POF-Zn <sup>2+</sup> -I <sup>-</sup>	298	✓	-	-	-	<i>Green Chem.</i> , 2018, <b>20</b> , 5285. <sup>67</sup>
12.	PPS@COF-TpBpy-Cu	496	✓	-	-	-	<i>J. Am. Chem. Soc.</i> , 2016, <b>138</b> , 15790. <sup>68</sup>
13.	Cu-BTTri MOF	-	-	-	<i>P. aeruginosa</i>	-	<i>Adv. Funct. Mater.</i> , 2017, <b>27</b> , 1702255. <sup>69</sup>
14.	PCN-224-Ag-HA	1898	-	✓	✓	-	<i>Adv. Funct. Mater.</i> , 2019, <b>29</b> , 1808594. <sup>70</sup>
15.	GO-Ag-MOF	1-32	-	<i>B. subtilis</i>	✓	-	<i>Adv. Mater. Interfaces</i> , 2018, <b>5</b> , 1701365. <sup>71</sup>
16.	NU-1008	1400	✓	-	-	-	<i>Chem. Sci.</i> , 2019, <b>10</b> , 1186. <sup>72</sup>

**Table S8** Comparative account of biofilm disruption by POF2 and Zn/POF2 with some of the representative polymeric materials, MOFs, metal nanoparticles, and composite materials.

Entry	Materials	Structure	Surface area (m <sup>2</sup> g <sup>-1</sup> )	Biofilm disruption		Reference
				Gram-positive	Gram-negative	
1	POF2		490	×	<i>E. coli</i>	This work
	Zn/POF2	<ul style="list-style-type: none"> <li>• Cost-effective gram-scale synthesis</li> <li>• Highly robust porous framework</li> <li>• Recyclable</li> <li>• Biocompatible</li> </ul>	104	×	<i>E. coli</i>	
<b>Organic polymer-based materials</b>						
2	Quaternary-ammonium compounds tethered on hyperbranched polyurea (Si-HB-PEI <sup>+</sup> )		-	×	<i>P. aeruginosa</i>	<i>Adv. Funct. Mater.</i> , 2014, <b>24</b> , 346. <sup>73</sup>
3	Poly-[[[(9,9-bis(6'- <i>N,N,N</i> -trimethylammonium)hexyl) fluorenylene phenylene]dibromide] (PFP)		-	<i>S. aureus</i>	×	<i>ACS Appl. Mater. Interfaces</i> 2017, <b>9</b> , 16933. <sup>74</sup>
4	Copolymerization of <i>N</i> -acryloyl-3-aminophenylboronic acid glucose ester with <i>N</i> -vinyl-2-pyrrolidone and <i>N</i> -isopropylacrylamide		-	×	<i>E. coli</i>	<i>Chem. Eur. J.</i> , 2017, <b>23</b> , 14883. <sup>75</sup>
5	Cationic homopolymer PE <sub>0</sub> and copolymer PE <sub>31</sub> containing 31 mol % of ethyl methacrylate		-	<i>S. mutans</i>	×	<i>Biomacromolecules</i> 2017, <b>18</b> , 257. <sup>76</sup>

7	Silicon(IV) phthalocyanine anchored poly(vinyl alcohol)		-	<i>E. coli</i>	×	<i>Angew. Chem. Int. Ed.</i> , 2017, <b>56</b> , 10362. <sup>77</sup>
8	Nitric oxide-loaded antimicrobial polymer		-	×	<i>P. aeruginosa</i>	<i>ACS Macro Lett.</i> , 2018, <b>7</b> , 592. <sup>78</sup>
9	Porphyrin-based POP		875	×	<i>S. aureus</i>	<i>ACS Appl. Bio Mater.</i> , 2019, <b>2</b> , 613. <sup>79</sup>
10	Quaternary polyethylenimine (QPEI) polymers with an amide or ester group in their pendant alkyl chain		-	<i>S. aureus</i>	<i>E. coli</i>	<i>ACS Appl. Mater. Interfaces</i> 2019, <b>11</b> , 39150. <sup>80</sup>
11	Fluorescent-conjugated polymer nanoparticles (PFPPBA)		-	×	<i>P. aeruginosa</i>	<i>Chem. Mater.</i> , 2020, <b>32</b> , 438. <sup>81</sup>
<b>Metal organic frameworks, composite materials and metal nanoparticles</b>						
12	Graphitic carbon nitride by embedded Ag nanoparticles	-	-	<i>S. aureus</i>	<i>E. coli</i>	<i>Nano Res.</i> 2015, <b>8</b> , 1648. <sup>82</sup>
13	Fe-terephthalate MIL-88B(Fe)	-	-	×	<i>S. typhimurium</i>	<i>ACS Appl. Mater. Interfaces</i> 2017, <b>9</b> , 4440–4449. <sup>83</sup>
14	Surface-adaptive gold nanoparticles (AuNPs)	-	-	<i>S. aureus</i>	×	<i>ACS Nano</i> 2017, <b>11</b> , 9330–9339. <sup>84</sup>

16	ZIF-8 nanoparticles, polyvinylidene fluoride (PVDF) perfluorooctyltriethoxysilane (POTS) composite PVDF/ZIF-8/POTS (PZP)	-	-	×	<i>E. coli</i>	<i>Adv. Mater. Interfaces</i> 2018, <b>5</b> , 1800167. <sup>85</sup>
17	PVA/CeO <sub>2-x</sub> NR composites	-	-	×	<i>E. coli</i>	<i>ACS Appl. Mater. Interfaces</i> 2018, <b>10</b> , 44722. <sup>86</sup>
18	MOF/Ce-based nanozymes	-	-	<i>S. aureus</i>	×	<i>Biomaterials</i> 2019, <b>208</b> , 21. <sup>87</sup>
19	CeO <sub>2</sub> -decorated porphyrin-based MOF	-	~ 2600	<i>S. aureus</i>	×	<i>Small</i> 2019, <b>15</b> , 1902522. <sup>88</sup>

## VII. Nuclear magnetic resonance (NMR) spectroscopy

### i. Solid-state $^{13}\text{C}$ CP-MAS NMR spectroscopic analysis of POF and Zn/POF

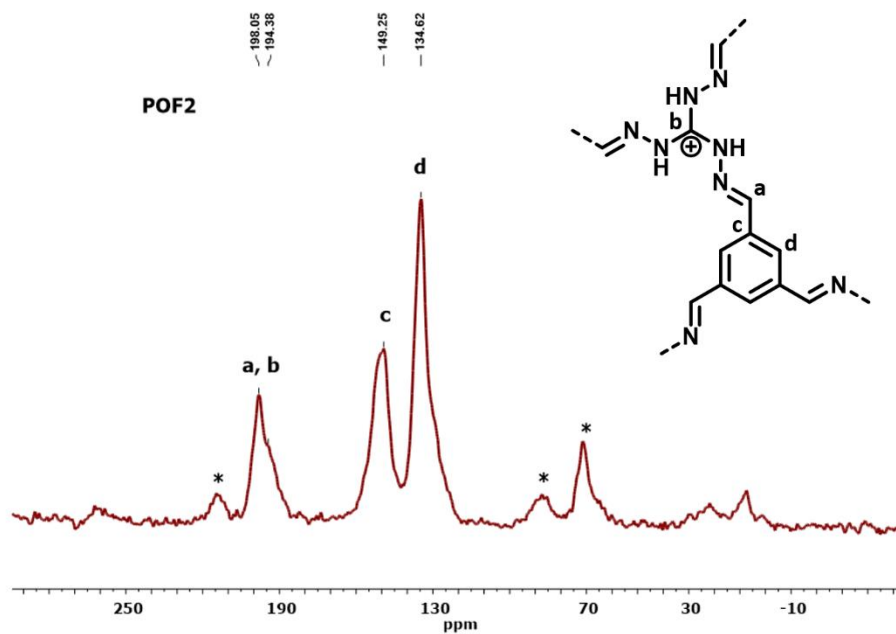


**Fig. S41** The solid-state  $^{13}\text{C}$  NMR spectrum of POF2; \*denotes the unassigned peaks.

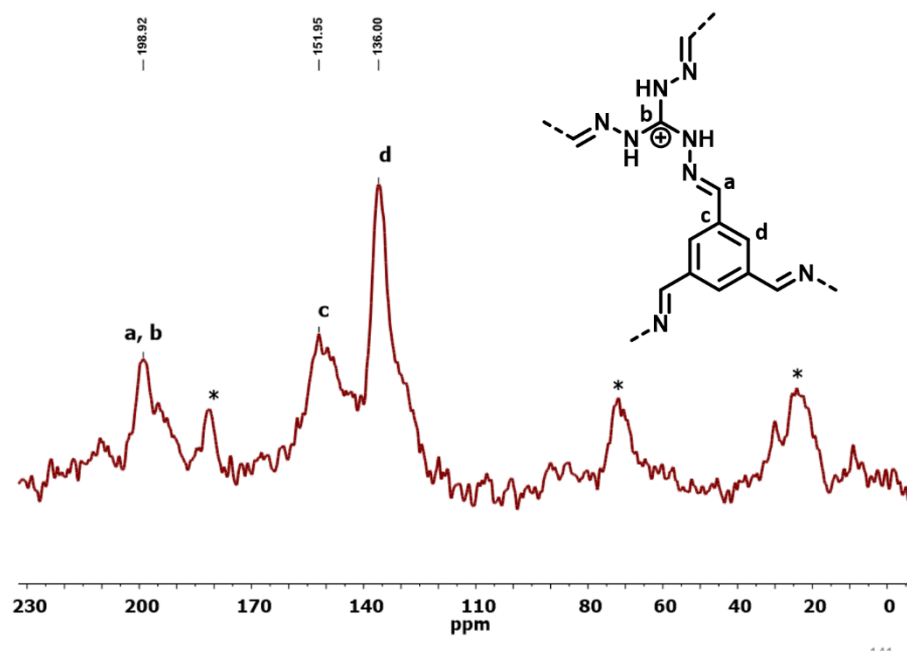


**Fig. S42** The solid-state  $^{13}\text{C}$  NMR spectrum of Zn/POF2; \*denotes the unassigned peaks.

## ii. NMR spectroscopic analysis of model compound (MTAG)

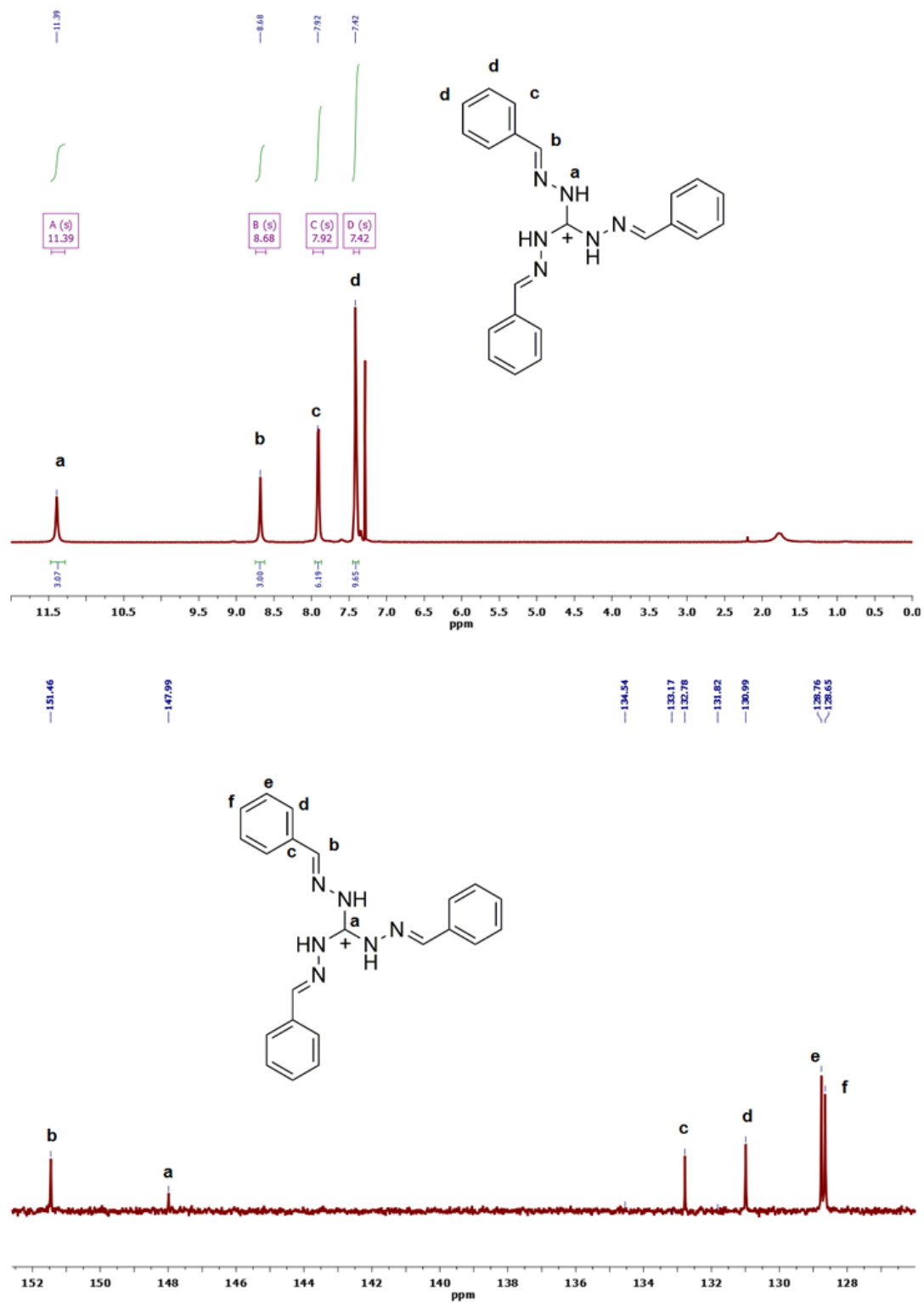
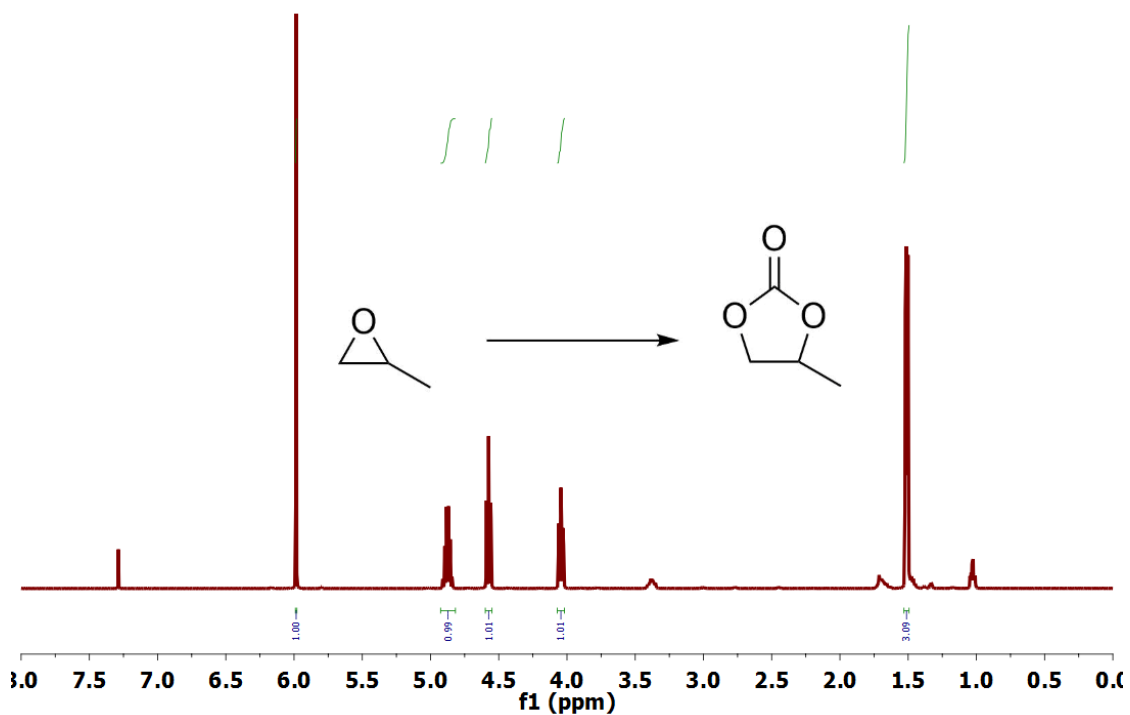
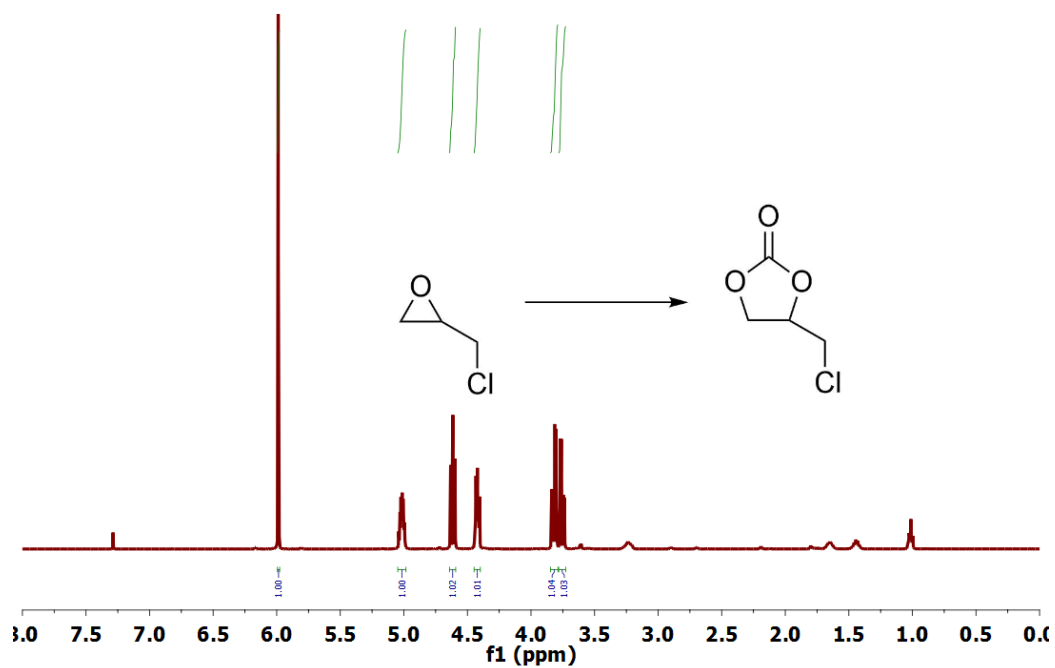


Fig. S43  $^1\text{H}$  (top) and  $^{13}\text{C}$  (bottom) NMR spectra ( $\text{CDCl}_3$ ) of the model compound (MTAG).



**Fig. S44** <sup>1</sup>H NMR spectrum of the reaction mixture (in CDCl<sub>3</sub>) for the conversion of propylene oxide with Zn/POF<sub>2</sub> as catalyst using 1,1,2,2-tetrachloroethane as external NMR standard.



**Fig. S45** <sup>1</sup>H NMR spectrum of the reaction mixture (in CDCl<sub>3</sub>) for the conversion of epichlorohydrin with Zn/POF<sub>2</sub> as catalyst using 1,1,2,2-tetrachloroethane as external NMR standard.



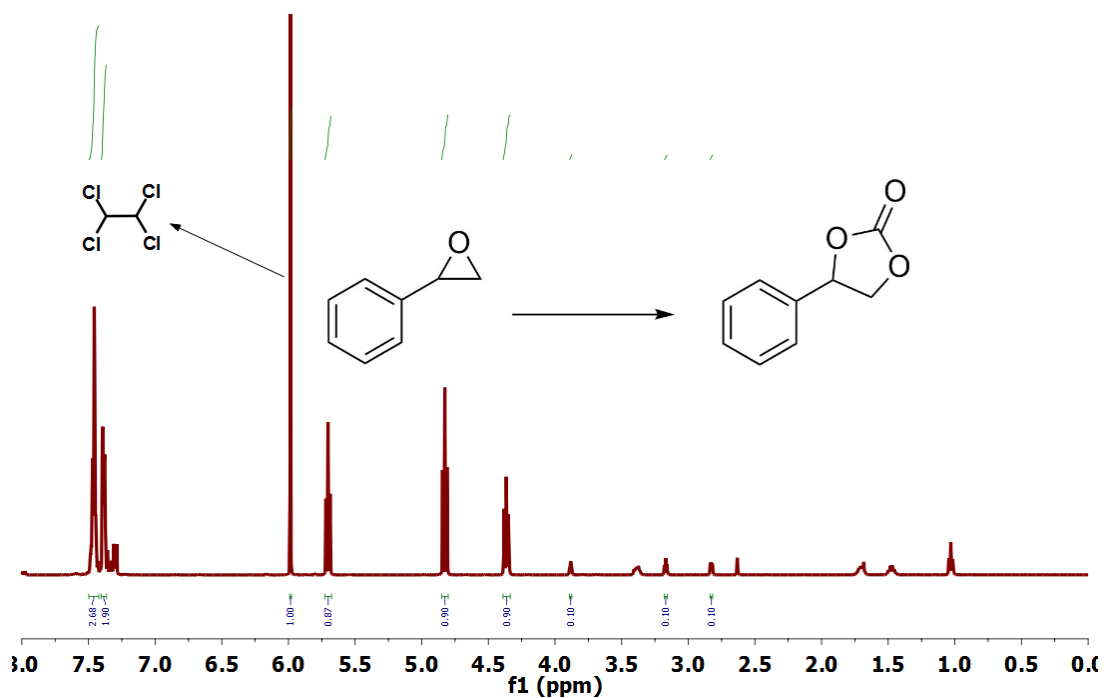


**Fig. S46**  $^1\text{H}$  NMR spectrum of the reaction mixture (in  $\text{CDCl}_3$ ) for the conversion of styrene oxide with  $\text{Zn}/\text{POF}_2$  as catalyst using *1,1,2,2*-tetrachloroethane as external NMR standard.

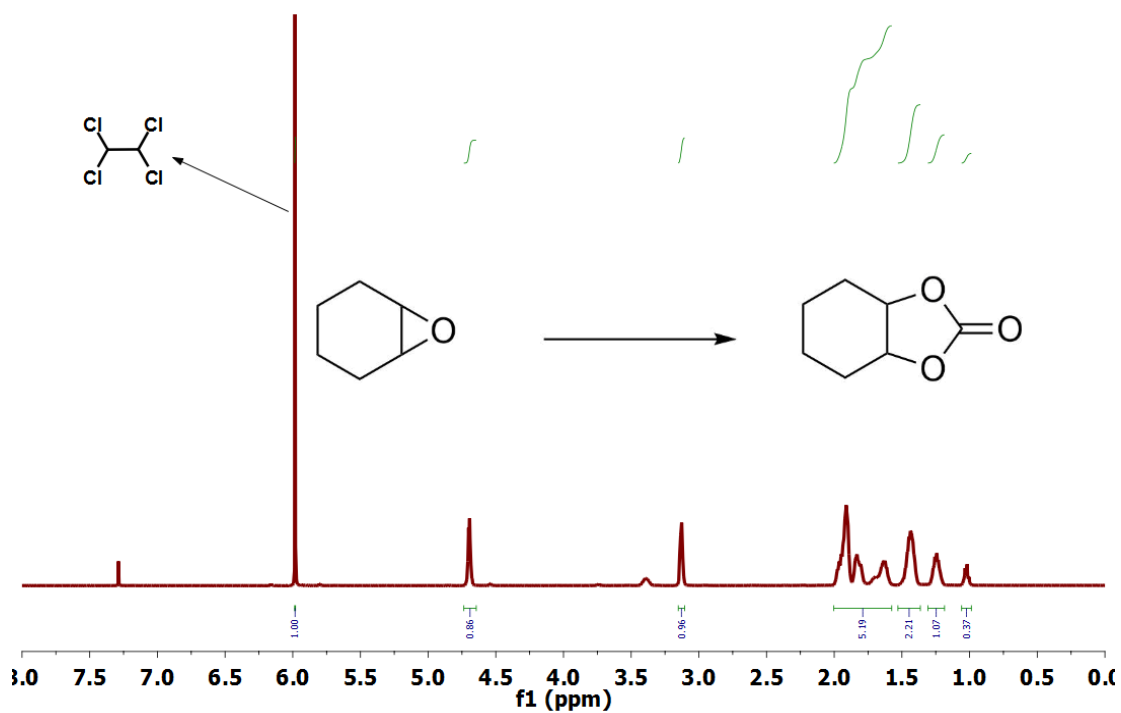


**Fig. S47**  $^1\text{H}$  NMR spectrum of the reaction mixture (in  $\text{CDCl}_3$ ) for the conversion of cyclohexene oxide with  $\text{Zn}/\text{POF}_2$  as catalyst using *1,1,2,2*-tetrachloroethane as external NMR standard.

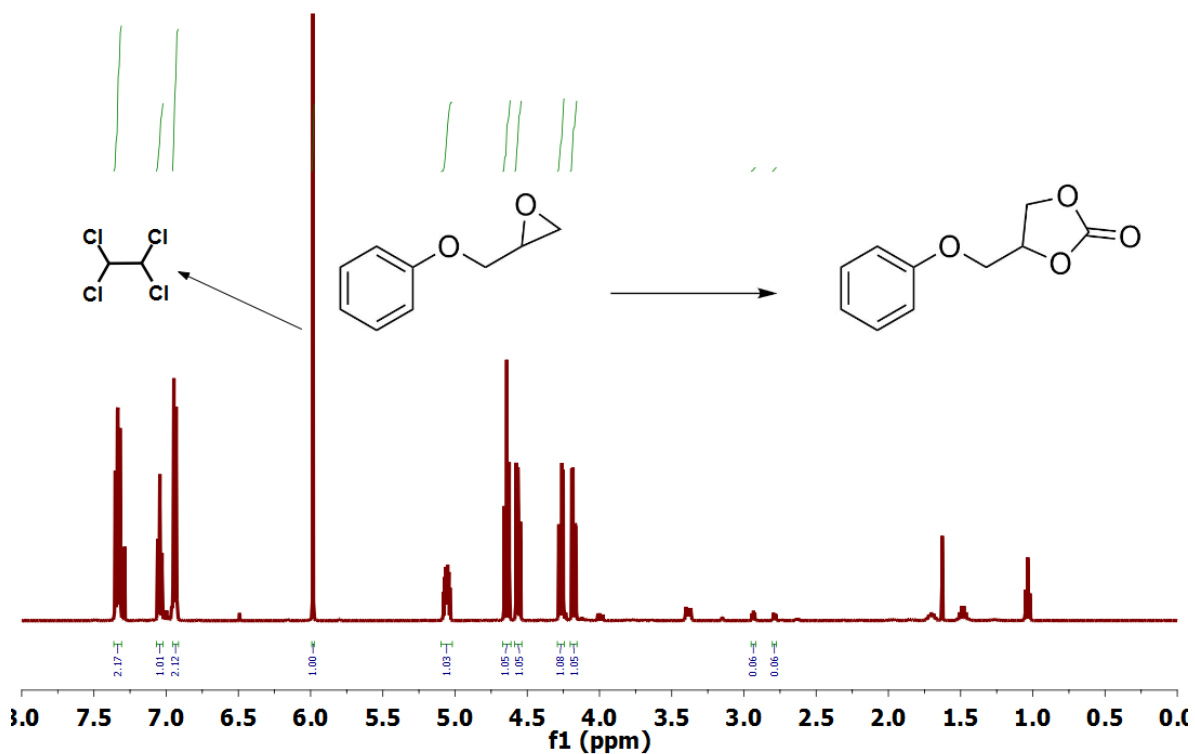


**Fig. S48** <sup>1</sup>H NMR spectrum of the reaction mixture (in CDCl<sub>3</sub>) for the conversion of 1,2-epoxy-3-phenoxypropane with Zn/POF<sub>2</sub> as catalyst using 1,1,2,2-tetrachloroethane as external NMR standard.

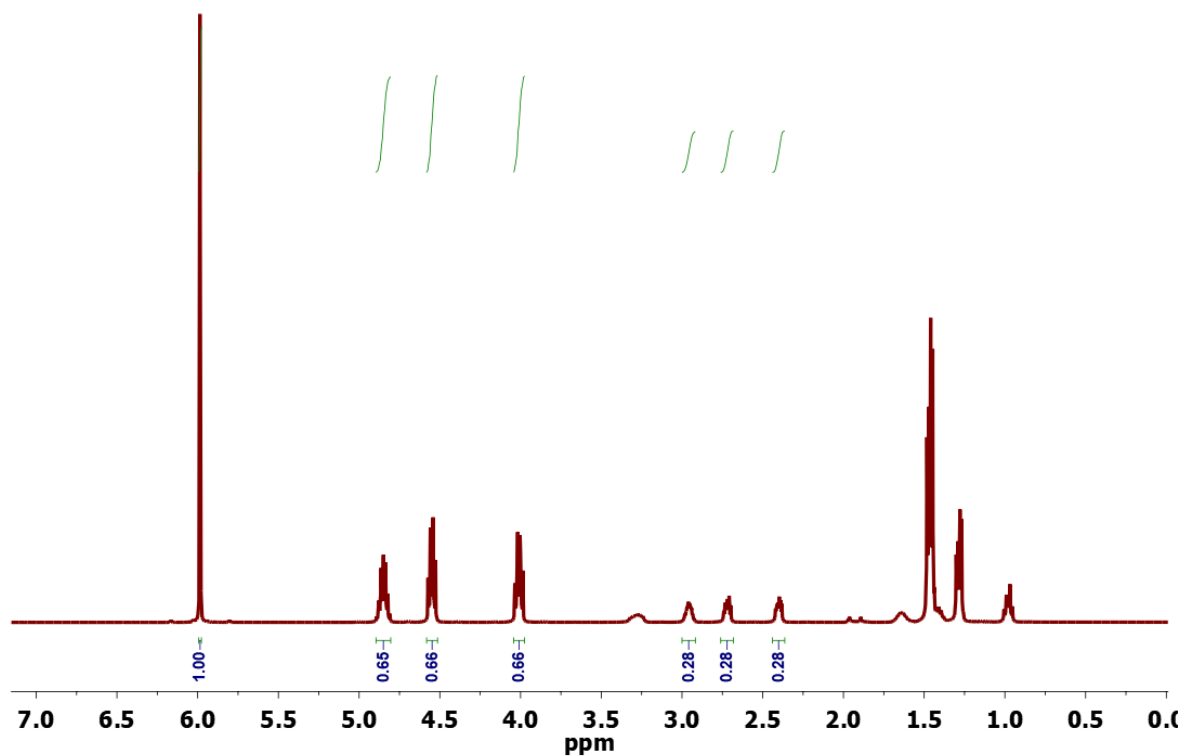


**Fig. S49** <sup>1</sup>H NMR spectrum of the reaction mixture (in CDCl<sub>3</sub>) for the conversion of propylene oxide with bulk ZnO using 1,1,2,2-tetrachloroethane as external NMR standard (indicating 65% conversion).

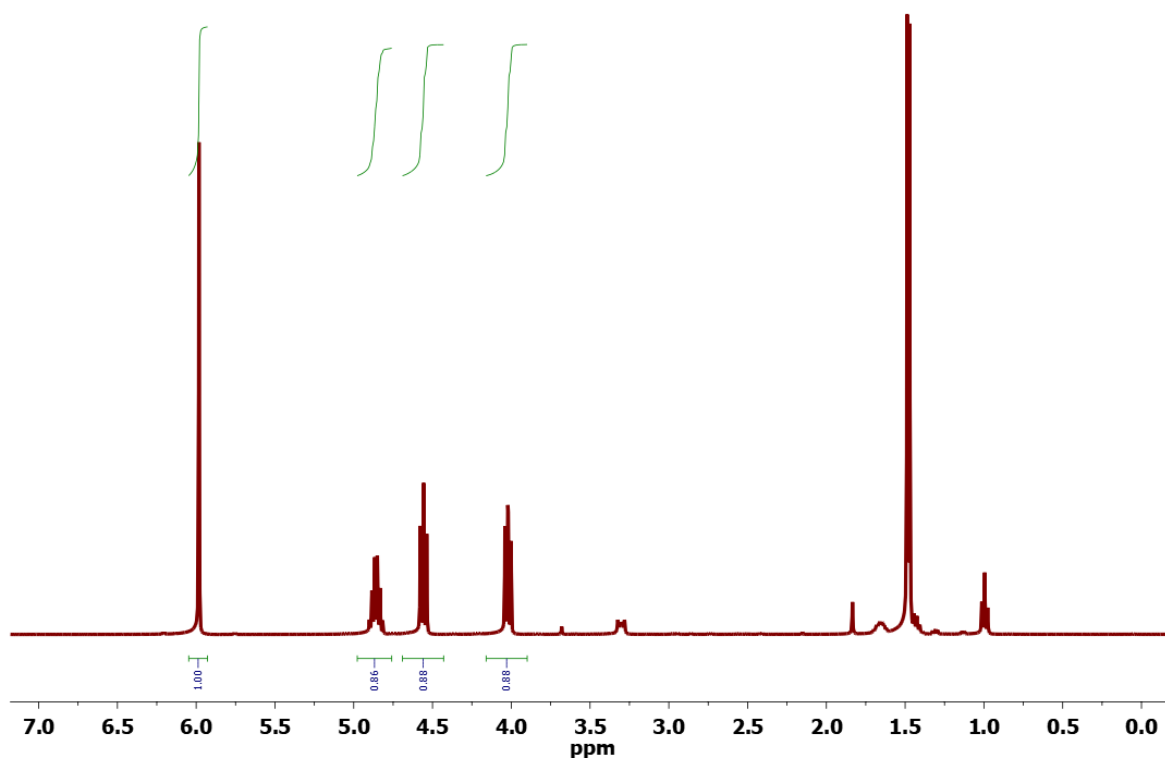


**Fig. S50**  $^1\text{H}$  NMR spectrum of the reaction mixture (in  $\text{CDCl}_3$ ) for the conversion of propylene oxide with ZnO nanoparticles using *1,1,2,2*-tetrachloroethane as external NMR standard (indicating 85% conversion).

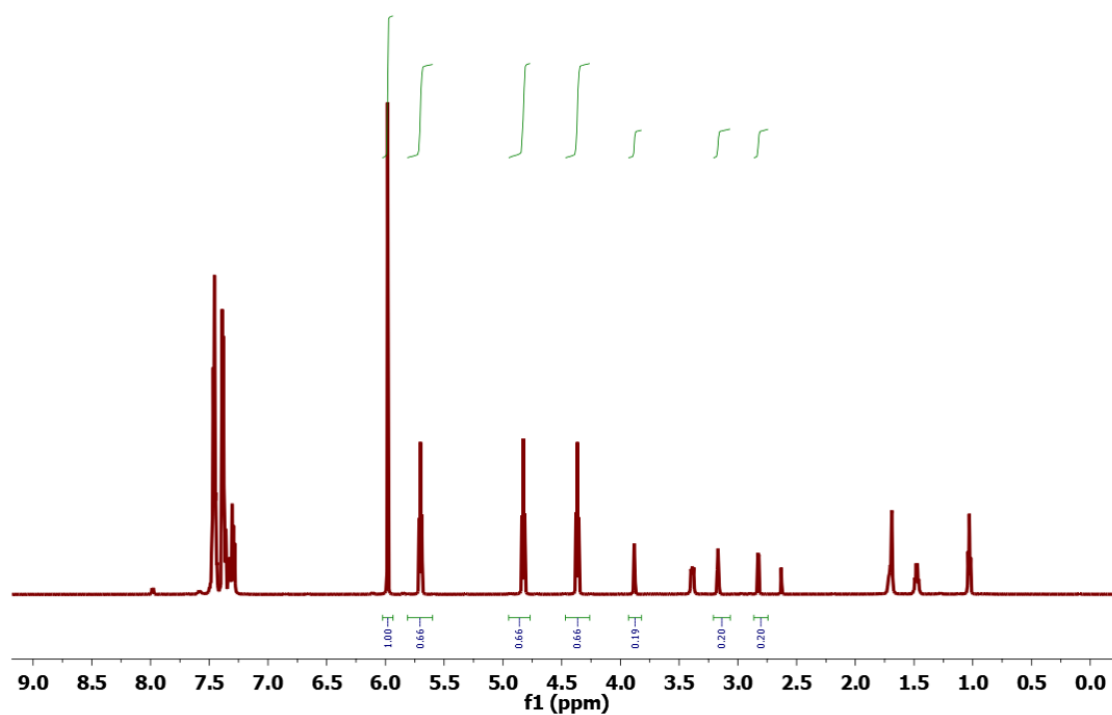


**Fig. S51**  $^1\text{H}$  NMR spectrum of the reaction mixture (in  $\text{CDCl}_3$ ) for the conversion of styrene oxide with ZnO nanoparticles using *1,1,2,2*-tetrachloroethane as external NMR standard (indicating 66% conversion).

## VIII. References

---

1. P. Pallavi, V. Kumar, MD. W. Hussain and A. Patra, *ACS Appl. Mater. Interfaces*, 2018, **10**, 44696.
2. S. Mitra, S. Kandambeth, B. P. Biswal, M. A. Khayum, C. K. Choudhury, M. Mehta, G. Kaur, S. Banerjee, A. Prabhune, S. Verma, S. Roy, U. K. Kharu and R. Banerjee, *J. Am. Chem. Soc.*, 2016, **138**, 2823.
3. G. Das, S. Nagaraja, V. Sridurai, D. B. Shinde, M. Addicoat, T. Prakasam, F. Gandara, F. Ravaux, S. K. Sharma, G. G. Nair, Z. Lai, R. Jagannathan, M. A. Olson and A. Trabolsi, *Chem. Mater.*, 2019, **31**, 4148.
4. (a) I. M. Müller and R. Robson, *Angew. Chem., Int. Ed.*, 2000, **39**, 4357; (b) B Ludi and M. Niederberger, *Dalton Trans.*, 2013, **42**, 12554; (c) V. Kumar, B. Sk, S. Kundu and A. Patra, *J. Mater. Chem. C*, 2018, **6**, 12086.
5. (a) S. Lee, S. Jeong, D. Kim, S. Hwang, M. Jeon and J. Moon, *Superlattices Microstruct.*, 2008, **43**, 330; (b) M. Wang, A. D. Li, J. Z. Kong, Y. P. Gong, C. Zhao, Y. F. Tang and D. Wu, *Nanoscale Res. Lett.*, 2018, **13**, 47; (c) P. Ingale, K. Knemeyer, M. P. Hermida, R. N. d'Alnoncourt, A. Thomas and F. Rosowski, *Nanomaterials*, 2020, **10**, 981.
6. (a) W. Li, Y. Zhuang, J. Wang, T. Yang, Y. Yu, M. Chen and J. Wang, *ACS Appl. Polym. Mater.*, 2019, **1**, 2797; (b) S. Venkateswarlu, A. Panda, E. Kim and M. Yoon, *ACS Appl. Nano Mater.*, 2018, **1**, 4198; (c) J. Wu, Y. Lin, J. Wang, P. Chang, C. Tasi, C. Lu, H. Chiu and Y. Yang, *Inorg. Chem.* 2003, **42**, 4516–4518; (d) X. Jiang, M. Li, H. Lu, L. Xu, H. Xu, S. Zang, M. Tang, H. Hou and T. C. W. Mak, *Inorg. Chem.*, 2014, **53**, 12665.
7. M. Thommes, K. Kaneko, A. V. Neimark, J. P. Olivier, F. Rodriguez-Reinoso, J. Rouquerol and K. S. W. Sing, *Pure Appl. Chem.*, 2015, **87**, 1051.
8. MD. W. Hussain, S. Bandyopadhyay and A. Patra, *Chem. Commun.*, 2017, **53**, 10576.
9. (a) J. Jeromenok and J. Weber, *Langmuir*, 2013, **29**, 12982; (b) Y. D. Cheng, L. Z. Zhai, M. M. Tong, T. Kundu, G. L. Liu, Y. P. Ying, J. Q. Dong, Y. X. Wang and D. Zhao, *ACS Sustainable Chem. Eng.*, 2019, **7**, 1564.
10. (a) A. L. Koch, *Anal. Biochem.*, 1970, **38**, 252; (b) B. D. Jett, K. L. Hatter, M. M. Huycke and M. S. Gilmore, *BioTechniques*, 1997, **23**, 648.
11. I. Sondi and B. Salopek-Sondi, *J. Colloid Interface Sci.*, 2004, **275**, 177.
12. Y. Chao and T. Zhang, *Appl. Microbiol. Biotechnol.*, 2011, **92**, 381.
13. S. N. Rampersad, *Sensors*, 2012, **12**, 12347.
14. J. H. Merritt, D. E. Kadouri and G. A. O'Toole, *Curr. Protoc. Microbiol.*, 2005, **00**, 1B.1.1.
15. G. Grégori, S. Citterio, A. Ghiani, M. Labra, S. Sgorbati, S. Brown and M. Denis, *Appl. Environ. Microbiol.*, 2001, **67**, 4662.
16. M. Berney, F. Hammes, F. Bosshard, H. U. Weilenmann and T. Egli, *Appl. Environ. Microbiol.*, 2007, **73**, 3283.
17. M. M. Bradford, *Anal. Biochem.*, 1976, **72**, 248.
18. A. Rosa, A. Chande, S. Ziglio, V. D. Sanctis, R. Bertorelli, S. L. Goh, S. M. McCauley, A. Nowosielska, S. E. Antonarakis, J. Luban, F. A. Santoni and M. Pizzato, *Nature*, 2015, **526**, 212.
19. A. Chande, E. C. Cuccurullo, A. Rosa, S. Ziglio, S. Carpenter and M. Pizzato, *Proc. Nat. Acad. Sci.*, 2016, **113**, 13197.

20. M. R. Neagu, P. Ziegler, T. Pertel, C. Strambio-De-Castillia, C. Grütter, G. Martinetti, L. Mazzucchelli, M. Grütter, M. G. Manz and J. Luban, *J. Clin. Invest.*, 2009, **119**, 3035.
21. (a) M. Pizzato, O. Erlwein, D. Bonsall, S. Kaye, D. Muir and M. O. McClure, *J. Virol.*, 2009, **156**, 1; (b) J. Vermeire, E. Naessens, H. Vanderstraeten, A. Landi, V. Iannucci, A. Van Nuffel, T. Taghon, M. Pizzato and B. Verhasselt, *PLoS One*, 2012, **7**, e50859.
22. L. C. Crowley, B. J. Marfell, N. J. Waterhouse, *Cold Spring Harbor Protoc.*, **2016**, pdb.prot087205.
23. G. Ji, Z. Yang, H. Zhang, Y. Zhao, B. Yu, Z. Ma and Z. Liu, *Angew. Chem. Int. Ed.*, 2016, **55**, 9685.
24. Y. Yuan, F. Sun, F. Zhang, H. Ren, M. Guo, K. Cai, X. Jing, X. Gao and G. Zhu, *Adv. Mater.*, 2013, **25**, 6619.
25. Y. Xie, T. T. Wang, X. H. Liu, K. Zou and W. Q. Deng, *Nat. Commun.*, 2013, **4**.
26. W. Wang, C. Li, L. Yan, Y. Wang, M. Jiang and Y. Ding, *ACS Catal.*, 2016, **6**, 6091.
27. Z. Z. Yang, B. Yu, H. Y. Zhang, Y. F. Zhao, Y. Chen, Z. S. Ma, G. P. Ji, X. Gao, B. X. Han and Z. M. Liu, *ACS Catal.*, 2016, **6**, 1268.
28. J. Chen, H. Li, M. M. Zhong and Q. H. Yang, *Green Chem.*, 2016, **18**, 6493.
29. M. Wu, Y. Han, B. Wang, Y. Yuan, C. Xing and Y. Chen, *ACS Appl. Bio Mater.*, 2018, **1**, 473.
30. S. Y. Ding, J. Gao, Q. Wang, Y. Zhang, W. G. Song, C. Y. Su and W. Wang, *J. Am. Chem. Soc.*, 2011, **133**, 19816.
31. S. L. Lu, Y. M. Hu, S. Wan, R. McCaffrey, Y. H. Jin, H. W. Gu and W. Zhang, *J. Am. Chem. Soc.*, 2017, **139**, 17082.
32. D. Chakraborty, S. Nandi, D. Mullangi, S. Halder, C. P. Vinod and R. Vaidhyanathan, *ACS Appl. Mater. Interfaces*, 2019, **11**, 15670.
33. D. Mullangi, D. Chakraborty, A. Pradeep, V. Koshti, C. P. Vinod, S. Panja, S. Nair and R. Vaidhyanathan, *Small*, 2018, **14**, 1801233.
34. H. Tian, F. Huang, Y. H. Zhu, S. M. Liu, Y. Han, M. Jaroniec, Q. H. Yang, H. Y. Liu, G. Q. M. Lu and J. Liu, *Adv. Funct. Mater.*, 2018, **28**, 1801737.
35. D. Zhao, Y. Li, S. Han, Y. Zhang, G. Jiang, Y. Wang, K. Guo, Z. Zhao, C. Xu, R. Li, C. Yu, J. Zhang, B. Ge and E. V. Kondratenko, *iScience*, 2019, **13**, 269.
36. S. Hermes, M. K. Schroter, R. Schmid, L. Khodeir, M. Muhler, A. Tissler, R. W. Fischer and R. A. Fischer, *Angew. Chem. Int. Ed.*, 2005, **44**, 6237.
37. M. Muller, S. Hermes, K. Kaehler, M. W. E. van den Berg, M. Muhler and R. A. Fischer, *Chem. Mater.*, 2008, **20**, 4576.
38. F. Chen, K. Shen, J. Chen, X. Yang, J. Cui and Y. Li, *ACS Cent. Sci.*, 2019, **5**, 176.
39. J. Rintjema, R. Epping, G. Fiorani, E. Martín, E. C. Escudero-Adán and A. W. Kleij, *Angew. Chem. Int. Ed.*, 2016, **55**, 3972.
40. F. Zhou, S. Xie, X. Gao, R. Zhang, C. Wang, G. Yin and J. Zhou, *Green Chem.*, 2017, **19**, 3908.
41. S. Sopeña, E. Martín, E. C. Escudero-Adán and A. W. Kleij, *ACS Catal.* 2017, **7**, 3532.
42. D. Kim, D. W. Kim, O. Buyukcakir, M. Kim, K. Polychronopoulou and A. Coskun, *Adv. Funct. Mater.*, 2017, **27**, 1700706.
43. P. Li, X. Wang, J. Liu, H. S. Phang, Y. Li and Y. Zhao, *Chem. Mater.*, 2017, **29**, 9256
44. P. Y. Wu, Y. Li, J. J. Zheng, N. Hosono, K. Otake, J. Wang, Y. H. Liu, L. L. Xia, M. Jiang, S. Sakaki and S. Kitagawa, *Nat. Commun.*, 2019, **10**, 4362.
45. K. Cho, S. M. Lee, H. J. Kim, Y. Ko, E. J. Kang and S. U. Son, *Chem. Eur. J.*, 2020, **26**, 788.

46. X. Wang, Y. Zhou, Z. Guo, G. Chen, J. Li, Y. Shi, Y. Liu and J. Wang, *Chem. Sci.*, 2015, **6**, 6916.
47. S. M. Sadeghzadeh, *Green Chem.*, 2015, **17**, 3059.
48. C. K. Ng, R. W. Toh, T. T. Lin, H. Luo, T. S. A. Hor and J. Wu, *Chem. Sci.*, 2019, **10**, 1549.
49. MD. W. Hussain, A. Giri and A. Patra, *Sustainable Energy Fuels*, 2019, **3**, 2567.
50. J. H. Lee, A. S. Lee, J. Lee, S. M. Hong, S. S. Hwang and C. M. Koo, *ACS Appl. Mater. Interfaces*, 2017, **9**, 3616.
51. Q. Su, Y. Qi, X. Yao, W. Cheng, L. Dong, S. Chen and S. Zhang, *Green Chem.*, 2018, **20**, 3232.
52. C. Calabrese, L. F. Liotta, F. Giacalone, M. Gruttadauria, C. Aprile, *ChemCatChem*, 2019, **11**, 560.
53. Y. Xie, T. T. Wang, X. H. Liu, K. Zou and W. Q. Deng, *Nat. Commun.*, 2013, **4**, 1960.
54. F. Liu, K. Huang, Q. Wu and S. Dai, *Adv. Mater.*, 2017, **29**, 1700445.
55. A. Giri, MD. W. Hussain, B. Sk and A. Patra, *Chem. Mater.*, 2019, **31**, 8440.
56. S. N. Talapaneni, O. Buyukcakir, S. H. Je, S. Srinivasan, Y. Seo, K. Polychronopoulou and A. Coskun, *Chem. Mater.*, 2015, **27**, 6818.
57. D. Ma, J. Li, K. Liu, B. Li, C. Li and Z. Shi, *Green Chem.*, 2018, **20**, 5285.
58. S. Subramanian, J. Oppenheim, D. Kim, T. S. Nguyen, W. M. H. Silo, B. Kim, W. A. Goddard and C. T. Yavuz, *Chem*, 2019, **5**, 3232.
59. C. Cui, R. Sa, Z. Hong, H. Zhong, R. Wang, *ChemSusChem*, 2020, **13**, 180.
60. R. Luo, X. Liu, M. Chen, B. Liu and Y. Fang, *ChemSusChem* 10.1002/cssc.202001079.
61. W. Miao, J. Wang, J. Liu and Y. Zhang, *Adv. Mater. Interfaces*, 2018, **5**, 1800167.
62. M. Liu, L. Wang, X. Zheng and Z. Xie, *ACS Appl. Mater. Interfaces*, 2017, **9**, 41512.
63. J. Wang, Y. Wang, Y. Zhang, A. Uliana, J. Zhu, J. Liu and B. Van der Bruggen, *ACS Appl. Mater. Interfaces*, 2016, **8**, 25508.
64. W. Zhou, S. Begum, Z. Wang, P. Krolla, D. Wagner, S. Bräse, C. Wöll and M. Tsotsalass, *ACS Appl. Mater. Interfaces*, 2018, **10**, 1528.
65. Q. Zhao, J. Hou, J. Shen, J. Liu and Y. Zhang, *J. Mater. Chem. A*, 2015, **3**, 18696.
66. O. Buyukcakir, S. H. Je, S. N. Talapaneni, D. Kim and A. Coskun, *ACS Appl. Mater. Interfaces*, 2017, **9**, 7209.
67. Q. Yang, J. Chen, M. Zhong, L. Tao, L. Liu, S. Jayakumar, H. Li and C. Li, *Green Chem.*, 2018, **20**, 903.
68. Q. Sun, B. Aguila, J. Perman, N. Nguyen and S. Ma, *J. Am. Chem. Soc.*, 2016, **138**, 15790.
69. B. H. Neufeld, M. J. Neufeld, A. Lutzke, S. M. Schweickart and M. M. Reynolds, *Adv. Funct. Mater.*, 2017, **27**, 1702255.
70. Y. Zhang, P. Sun, L. Zhang, Z. Wang, F. Wang, K. Dong, Z. Liu, J. Ren, X. Qu, *Adv. Funct. Mater.*, 2019, **29**, 1808594.
71. M. D. Firouzjaei, A. A. Shamsabadi, M. S. Gh., A. Rahimpour and M. Soroush, *Adv. Mater. Interfaces*, 2018, **5**, 1701365.
72. J. F. Lyu, X. Zhang, K. Otake, X. J. Wang, P. Li, Z. Y. Li, Z. J. Chen, Y. Y. Zhang, M. C. Wasson, Y. Yang, P. Bai, X. H. Guo, T. Islamoglu and O. K. Farha, *Chem. Sci.*, 2019, **10**, 1186.
73. L. A. T. W. Asri, M. Crismaru, S. Roest, Y. Chen, O. Ivashenko, P. Rudolf, J. C. Tiller, H. C. V. D. Mei, T. J. A. Loontjens and H. J. Busscher, *Adv. Funct. Mater.* 2014, **24**, 346.
74. P. Zhang, S. Li, H. Chen, X. Wang, L. Liu, F. Lv and S. Wang, *ACS Appl. Mater. Interfaces* 2017, **9**, 16933.

75. C. Ding, Z. Yan, J. Ren and X. Qu, *Chem. Eur. J.* 2017, **23**, 14883.
76. H. Takahashi, E. T. Nadres and K. Kuroda, *Biomacromolecules* 2017, **18**, 257.
77. A. Galstyan, R. Schiller and U. Dobrindt, *Angew. Chem. Int. Ed.* 2017, **56**, 10362.
78. R. Namivandi-Zangeneh, Z. Sadrearhami, A. Bagheri, M. Sauvage-Nguyen, K. K. K. Ho, N. Kumar, E. H. H. Wong and C. Boyer, *ACS Macro Lett.* 2018, **7**, 592.
79. Z. Li, X. Feng, S. Gao, Y. Jin, W. Zhao, H. Liu, X. Yang, S. Hu, K. Cheng and J. Zhang, *ACS Appl. Bio Mater.* 2019, **2**, 613.
80. J. Hoque, P. Akkapeddi, C. Ghosh, D. S. S. M. Uppu and J. Haldar, *ACS Appl. Mater. Interfaces* 2019, **11**, 39150.
81. L. Liu, X. Wang, S. Zhu, C. Yao, D. Ban, R. Liu, L. Li and S. Wang, *Chem. Mater.* 2020, **32**, 438.
82. W. Bing, Z. Chen, H. Sun, P. Shi, N. Gao, J. Ren and X. Qu, *Nano Res.* 2015, **8**, 1648.
83. B. Claes, T. Boudewijns, L. Muchez, G. Hooyberghs, E. V. V. Eycken, J. Vanderleyden, H. P. Steenackers and D. E. D. Vos, *ACS Appl. Mater. Interfaces* 2017, **9**, 4440.
84. D. Hu, H. Li, B. Wang, Z. Ye, W. Lei, F. Jia, Q. Jin, K. Ren and J. Ji, *ACS Nano* 2017, **11**, 9330.
85. W. Miao, J. Wang, J. Liu and Y. Zhang, *Adv. Mater. Interfaces* 2018, **5**, 1800167.
86. M. Hu, K. Korschelt, M. Viel, N. Wiesmann, M. Kappl, J. Brieger, K. Landfester, H. Therien-Aubin and W. Tremel, *ACS Appl. Mater. Interfaces* 2018, **10**, 44722.
87. Z. Liu, F. Wang, J. Ren and X. Qu, *Biomaterials* 2019, **208**, 21.
88. H. Qiu, F. Pu, Z. Liu, Q. Q. Deng, P. Sun, J. Ren and X. Qu, *Small* 2019, **15**, 1902522.